



Time-Spectral Method for Overlapping Meshes

Joshua I. Leffell*

Stanford University, Stanford, California 94305

and

Scott M. Murman[†] and Thomas H. Pulliam[‡]

NASA Ames Research Center, Moffett Field, California 94035

DOI: 10.2514/1.J054850

Overset and Cartesian solvers typically employ conventional time-marching schemes to simulate unsteady flows. Temporal pseudospectral schemes have demonstrated the ability to dramatically reduce the computational effort required to resolve the important subclass of time-periodic phenomena. Incorporating the time-spectral method within these approaches is desirable, but direct application is infeasible. Relative motion introduces dynamic blanking of spatial nodes which move interior to solid bodies; the solution at such nodes is therefore undefined over specific intervals of time. This proves problematic for the conventional time-spectral method because it expands the temporal variation at every node as an infinitely supported Fourier series. An extension of the time-spectral method is presented where dynamically blanked nodes are handled in an alternative manner; the solution through intervals of consecutively unblanked time samples are represented with barycentric rational interpolants. The Fourier- and rational interpolant-based differentiation operators are applied in tandem, providing a hybrid time-spectral scheme capable of consistently resolving relative motion on overlapping meshes. The hybrid scheme is applied to relevant cases in two and three spatial dimensions and the results demonstrate that the hybrid scheme mirrors the performance of the conventional time-spectral method and monotonically converges to analogous high-resolution, time-accurate simulations with increasing temporal modes.

Nomenclature

a	=	plunge amplitude
C_Q	=	torque coefficient
C_T	=	thrust coefficient
c	=	chord length
c_d	=	sectional drag coefficient
\mathcal{D}_N	=	differentiation operator
D_N	=	global temporal differentiation operator
d	=	barycentric rational interpolant approximation order
d_{\max}	=	barycentric rational interpolant approximation order limit
h	=	nondimensional plunge amplitude, where h is equal to a/c
I_N	=	interpolation operator
i	=	imaginary unit, $\sqrt{-1}$
K	=	number of temporal modes, where K equals $(N - 1)/2$
k	=	reduced frequency, where k equals $\omega c/V_\infty$
M	=	Mach number
N	=	number of temporal degrees of freedom
N_Q	=	number of conserved quantities
N_{SD}	=	number of spatial dimensions
N_x	=	number of spatial degrees of freedom
Re	=	Reynolds number
St	=	Strouhal number, where St is equal to kh
T	=	temporal period
t	=	physical time
\tilde{u}_k	=	k th frequency component of u vector

α	=	pitch incidence
δ_x	=	general finite difference operator in the x direction
θ	=	pitch amplitude
μ	=	advance ratio
$\tilde{\nu}$	=	undamped eddy viscosity
τ	=	pseudotime
ϕ_k	=	basis function corresponding to the k th mode or node
Ψ	=	azimuthal angle
ψ_k	=	test function corresponding to the k th mode or node
ω	=	fundamental frequency

Subscripts

tip	=	tip value
∞	=	freestream value

Superscripts

n	=	physical time index
s	=	iteration index

I. Introduction

FORCED periodic flows arise in a broad range of aerodynamic applications, such as rotorcraft, turbomachinery, and flapping-wing configurations. The standard procedure for simulating such flows involves advancing the unsteady governing equations forward in time long enough for the initial transient to exit the computational domain and to ultimately achieve a statistically stationary flow. It is often necessary to simulate several periods of motion to accomplish this task, making unsteady design optimization prohibitively expensive for many realistic problems. An effort to reduce the computational expense of these calculations led to the development of a harmonic balance method applied to the Navier–Stokes equations by Hall et al. [1,2], which capitalizes on the periodic nature of the solution while maintaining the ability to resolve nonlinearities inherent in the underlying physics. This approach exploits the fact that time-periodic flow, while varying in the time domain, remains invariant in the frequency domain. Expanding the temporal variation at each spatial node as a truncated Fourier series transforms the unsteady governing equations into a coupled set of steady equations in integer harmonics that can be tackled with the acceleration techniques commonly

Received 8 March 2016; revision received 23 December 2016; accepted for publication 28 February 2017; published online 29 September 2017. Copyright © 2017 by the American Institute of Aeronautics and Astronautics, Inc. All rights reserved. All requests for copying and permission to reprint should be submitted to CCC at www.copyright.com; employ the ISSN 0001-1452 (print) or 1533-385X (online) to initiate your request. See also AIAA Rights and Permissions www.aiaa.org/randp.

*Ph.D. Candidate, Department of Aeronautics & Astronautics; currently Senior Research Engineer, Computer Science Laboratory, SRI International; joshua.leffell@sri.com.

[†]Research Scientist, Computational Physics Branch, Mail Stop 258-5; Scott.M.Murman@nasa.gov. Member AIAA.

[‡]Senior Research Scientist, Computational Aerosciences Branch, Mail Stop 258-2; Thomas.H.Pulliam@nasa.gov. Associate Fellow AIAA.

afforded to steady-state flow solvers. Similar Fourier pseudospectral approaches, such as the nonlinear frequency domain [3–5], reduced-frequency [6], and time-spectral (TS) [7–9] methods, were also developed.

Temporal Fourier pseudospectral methods have demonstrated marked success in reducing the computational costs associated with simulating forced periodic flows [4]. In such an approach, the solutions at N equispaced time instances are coupled through an infinitely supported temporal differentiation operator. The trigonometric representation of periodic phenomena provides spectral convergence as the number of resolved harmonics K , and correspondingly, the number of time samples $N = 2K + 1$ increases. The spectral convergence rate of Fourier methods is superior to the algebraic convergence rates associated with traditional time-accurate (TA) schemes for unsteady calculations, implying that a given level of accuracy can be achieved with significantly fewer temporal degrees of freedom [10]. Some approaches iterate the equations in the frequency domain, whereas others operate entirely in the time domain to simplify the process of augmenting this capability within existing flow solvers. However, each approach harnesses the underlying steady solution in the frequency domain.

Cartesian and overlapping grid methodologies are versatile techniques capable of handling complex geometry configurations with relative motion between components and are commonly used for practical engineering applications. The combination of the time-spectral method with this general capability has the potential of providing an enabling design and analysis tool. In an arbitrary moving-body scenario for overset or Cartesian approaches, a Lagrangian body moves relative to a fixed Eulerian mesh (or another Lagrangian mesh). Mesh points interior to solid bodies are removed (cut), leaving a hole in the background mesh. Such points are excluded (blanked) from the computational domain over which the governing equations are solved, rendering the solution at such nodes as undefined. In general, such grid points undergo dynamic blanking, where their status is active for some subset of time and otherwise blanked. Dynamically blanked nodes lack a complete set of time samples, preventing direct application of the time-spectral method due to the infinite support of the complex exponential basis functions of the Fourier series, upon which the method is based. Murman [6] incorporated a temporal pseudospectral approach within a Cartesian solver with rigid domain motion, wherein the hole cutting remained fixed. Similarly, Thomas et al. [11,12] and Custer [13] applied the method within the NASA overset solver OVERFLOW with static hole cutting. Blanc et al. [14] implemented an iterative procedure to eliminate dynamically blanked nodes, if possible, to facilitate the use of the standard time-spectral method on dynamic overset grids. Soucy and Nadarajah [15] avoided dynamically blanked nodes by extending the near-body grids such that they envelop the solid body at all time instances. These approaches prove worthy for certain configurations but are not general solutions for the case of arbitrary relative motion. Mavriplis et al. [16] demonstrated a general approach to treat dynamically blanked nodes by applying a Laplacian operator to populate the blanked region with spatially smoothed data. In the current work, a hybrid time-spectral scheme capable of consistently treating dynamically blanked nodes resulting from general relative motion between overset grids is developed and implemented within the NASA Navier–Stokes solver OVERFLOW.

Background information on the time-spectral method and overset grid technology presented in Sec. II, provides context for Sec. III, which expounds the difficulty of applying the time-spectral method within the overset framework for arbitrary relative motion. Section III then introduces a strategy to resolve overset relative motion within the time-spectral methodology. NASA's OVERFLOW solver is described in Sec. IV, in addition to an overview of the modifications that were made to augment the solver with time-spectral capability; memory and computational overheads with respect to the steady-state solver are addressed. Numerical experiments presented in Sec. V demonstrate the viability of the proposed approach, including two-dimensional inviscid high-amplitude and turbulent Reynolds-averaged Navier–Stokes (RANS) high-speed oscillating airfoils and

the three-dimensional quarter-scale V-22 Tilt Rotor Aeroacoustic Model (TRAM) in hover and forward (edgewise) flight.

II. Background

Brief synopses of the conventional time-spectral method and overset grid methodology are provided before continuing with the proposed solution strategy of the current work.

A. Time-Spectral Method

The standard time-spectral method is derived as a Fourier collocation scheme [17,18] for a time-periodic solution u to a representative semidiscretized partial differential equation with a discrete spatial residual operator $\mathbf{R}(u)$, which is free to be of linear or nonlinear form:

$$\frac{d}{dt}u(\mathbf{x}, t) + \mathbf{R}(u(\mathbf{x}, t)) = 0 \quad (1)$$

The solution is assumed periodic in time a priori, such that $u(\mathbf{x}, t + T) = u(\mathbf{x}, t)$ for a given period T . It is therefore advantageous to express the solution at every point in space \mathbf{x} as a Fourier series whose basis functions $\phi_k(t) = e^{i\omega kt}$ are the complex exponentials in integer harmonics of the fundamental frequency $\omega = 2\pi/T$, which naturally satisfy periodicity:

$$u(\mathbf{x}, t) = \sum_{k=-\infty}^{\infty} \tilde{u}_k(\mathbf{x})\phi_k(t) \quad (2)$$

Truncating Eq. (2) to $N = 2K + 1$ terms retains K modes in the approximate solution u_N :

$$u_N(\mathbf{x}, t) = I_N u = \sum_{k=-K}^K \tilde{u}_k(\mathbf{x})\phi_k(t) \quad (3)$$

The method of weighted residuals is applied to approximate the solution by minimizing a discrete residual R_N of Eq. (1):

$$R_N(\mathbf{x}, t) = \frac{d}{dt}u_N(\mathbf{x}, t) + \mathbf{R}(u_N(\mathbf{x}, t)) \quad (4)$$

This approach requires that R_N integrates to zero against an appropriate set of test functions ψ over the period [19]:

$$(R_N, \psi_n)_w = \int_0^T R_N \psi_n w dt = 0, \quad n \in \{0, \dots, N-1\} \quad (5)$$

Selecting the test functions $\psi_n = \delta(t - t_n)$ with weighting $w = 1$ defines a collocation scheme because it eliminates the discrete residual at each of the N collocation points t_n :

$$\frac{d}{dt}u_N(\mathbf{x}, t_n) + \mathbf{R}(u_N(\mathbf{x}, t_n)) = 0, \quad n \in \{0, \dots, N-1\} \quad (6)$$

The collocation points are distributed uniformly over the period $t_n = nT/N$, providing discrete orthogonality for the trigonometric basis functions [19].

The temporal derivative in Eq. (6) is evaluated by analytically differentiating the truncated Fourier series in Eq. (3):

$$\frac{d}{dt}u_N(\mathbf{x}, t) = \sum_{k=-K}^K i\omega k \tilde{u}_k(\mathbf{x}) e^{i\omega kt} \quad (7)$$

The spatially varying Fourier coefficients $\tilde{u}_k(\mathbf{x})$ are determined by application of the discrete Fourier transform (DFT) to the solution values at the N collocation points $u_N^n(\mathbf{x}) = u_N(\mathbf{x}, t_n)$:

$$\tilde{u}_k(\mathbf{x}) = \frac{1}{N} \sum_{j=0}^{N-1} u_N^j(\mathbf{x}) e^{-i\omega k t_j} \quad (8)$$

Although application of the DFT results in a pseudospectral method, it enables the direct adoption of spatial operators from existing flow solvers as the spatial residual is evaluated in the time domain. Substitution of \tilde{u}_k in Eq. (8) into Eq. (7) defines the temporal derivative at a particular time sample t_n as a weighted sum of the solution at every other time sample ($d_n^n = 0$):

$$\frac{d}{dt} u_N^n(\mathbf{x}) = \sum_{k=-K}^K i\omega k \tilde{u}_k(\mathbf{x}) e^{i\omega k t_n} \quad (9)$$

$$= \sum_{j=0}^{N-1} \left(\frac{1}{N} \sum_{k=-K}^K i\omega k e^{i\omega k (t_n - t_j)} \right) u_N^j(\mathbf{x}) \quad (10)$$

$$= \sum_{j=0}^{N-1} d_j^n u_N^j(\mathbf{x}) \quad (11)$$

The time derivative can be evaluated at each collocation point and expressed in matrix form to define the Fourier interpolation derivative operator [20] \mathcal{D}_N , which acts on the time history of the solution $\mathbf{u}_N(\mathbf{x}) = \{u_N^0(\mathbf{x}), \dots, u_N^{N-1}(\mathbf{x})\}^T$:

$$\frac{d}{dt} \mathbf{u}_N(\mathbf{x}) = \mathcal{D}_N \mathbf{u}_N(\mathbf{x}) \quad (12)$$

The elements d_j^n of the temporal differentiation operator are included here for N odd [9]:

$$d_j^n = \begin{cases} \frac{\omega}{2} (-1)^{n-j} \csc\left(\frac{\pi(n-j)}{N}\right), & j \neq n \\ 0, & j = n \end{cases} \quad (13)$$

Replacing the analytic temporal derivative in Eq. (6) with the discrete approximation in Eq. (11) results in a steady system of equations spanning both time and space:

$$\sum_{j=0}^{N-1} d_j^n u_N^j + \mathbf{R}(u_N^n) = 0, \quad n \in \{0, \dots, N-1\} \quad (14)$$

Applying pseudotime continuation to Eq. (14) facilitates an iterative procedure reminiscent of conventional steady-state solvers:

$$\frac{d}{d\tau} u_N^n + \sum_{j=0}^{N-1} d_j^n u_N^j + \mathbf{R}(u_N^n) = 0, \quad n \in \{0, \dots, N-1\} \quad (15)$$

The discrete Fourier series in Eq. (3) can be used to reconstruct the solution at any point in continuous time upon satisfying Eq. (15).

B. Overset Grid Technology

The chimera grid approach was introduced to facilitate the use of efficient structured-grid algorithms on complex geometries by splitting the computational domain into a system of overlapping meshes [21]. In standard practice, curvilinear, body-fitted grids envelop the solid geometry and lie embedded within a system of background Cartesian grids. Mesh points interior to solid bodies are blanked and removed from the computational domain because the equations governing fluid dynamics are invalid at such locations. Overset grids, although separate logical entities, must be connected to facilitate communication across their boundary interfaces. This requires overlap regions for which size depends on the stencil of the numerical scheme. Fringe points are identified on the boundary of the overlap regions and tagged as receiver nodes. The domain connectivity software interpolates the solution from the donor grid in the vicinity of each fringe point to define the solution on boundary interfaces. This is repeated on all grids, ensuring that every boundary node is either populated with interpolated data from a neighboring zone or is defined through a physical or far-field boundary condition.

In a moving-body scenario, grids can either move together rigidly or relative to one another. For the case of rigid motion, where all grids move in unison, the blanking status for all mesh points remains constant in time, such that a spatial node whose solution is defined at one time is guaranteed to have a solution defined for all time. However, for the case of relative motion, where grids move independently, the blanking status of particular grid points may change over time. Consider the case of a plunging airfoil, where a curvilinear near-body grid wraps the body and is embedded within a background Cartesian grid. Figure 1 depicts the blanking status for the background Cartesian grid for both rigid and relative motion. The background grid is shown at three equispaced time instances over the period of oscillation. The blue-colored nodes are unblanked for every time instance and the white region corresponds to the hole cut at the particular time instance. For the case of rigid-body motion, depicted in Fig. 1a, the hole cut remains constant; every node that is unblanked at one time instance is unblanked for all three, which is not the case for the case of relative motion depicted in Fig. 1b. Because the airfoil grid moves relative to the stationary background grid, a different set of nodes are blanked at each time instance; some nodes are blanked at one time instance but unblanked at other time instances. The dynamically blanked nodes colored red in the figure only contain physically meaningful solution data at a subset of the three time samples.

Herein lies the fundamental difficulty of applying the time-spectral approach within an overset framework; complete time histories are not available for every grid point, thereby precluding a unique representation of the aperiodic solution at dynamically blanked nodes using the discrete Fourier analysis detailed earlier. The infinitely supported Fourier differentiation operator cannot be employed under such circumstances, and therefore, an alternative treatment is sought for such nodes.

III. Hybrid Time-Spectral Method

The fundamental obstacle of extending the time-spectral method to overset solvers emerges from nodes that dynamically move in and out

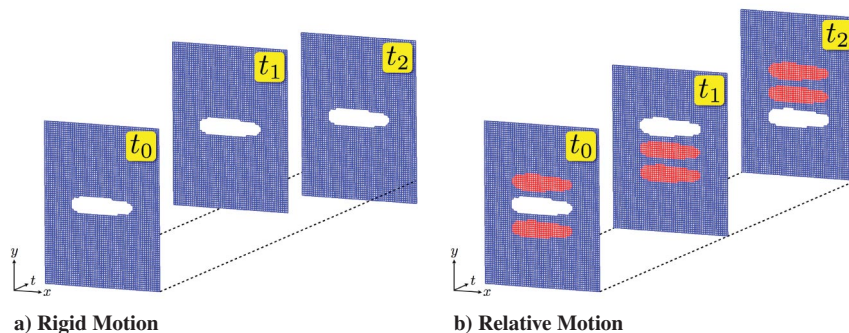


Fig. 1 Hole cut at three time instances for a plunging airfoil using both rigid and relative motion.

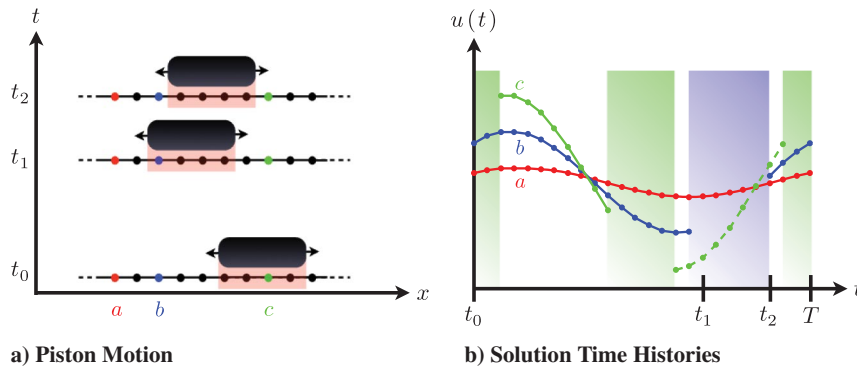


Fig. 2 Figurative a) piston trajectory and b) solution histories at nodes a , b , and c .

of the physical domain due to relative motion between grids and solid geometry. Such nodes lack a complete time history of N physical states at the N equispaced temporal collocation points, rendering the infinitely supported Fourier differentiation operator, and therefore the conventional time-spectral method, unsuitable. Thus, an alternative approach is required for representing the solution and, correspondingly, its temporal derivative, at the unblanked collocation points for nodes undergoing dynamic hole cutting. The primary objective of the current work is therefore to determine an appropriate differentiation operator at such nodes without sacrificing the spectral convergence afforded by the standard time-spectral method.

Figure 2 illustrates the issue at dynamically blanked nodes for a representative one-dimensional oscillating piston. Fictional solutions in Fig. 2b corresponding to nodes a , b , and c in Fig. 2a demonstrate dynamic hole cutting by the motion of the piston relative to the background Eulerian grid. Node a never lies within the piston, and therefore its solution is defined throughout the entire period. The piston blanks node b briefly and node c twice. Thus, node b has a single associated subperiodic time interval, whereas node c has two (one each represented by the solid and hashed lines in Fig. 2b). The shaded regions serve to highlight the time over which each node lies outside the physical domain (i.e., inside the impermeable boundary of the piston, lacking a physically meaningful solution). The standard time-spectral scheme can be applied to node a , whereas special treatment is required for nodes b and c .

Although the objective of the proposed approach is to successfully approximate the solution and temporal derivative at each dynamically blanked spatial node, it is critical to maintain the same equidistant time sampling used in the conventional time-spectral method. One of the more attractive features of the time-spectral method is the ability to incorporate its functionality into mature flow solvers with minimal effort by leveraging existing spatial operators [12]. Modifying the distribution of temporal collocation points at dynamically blanked nodes would necessitate an overhaul of the spatial residual operators; neighboring spatial mesh points would no longer be guaranteed to exist at the same location in time, which would require costly and potentially ill-conditioned temporal interpolation to evaluate spatial derivatives. Therefore, the distribution of evenly spaced collocation points is constrained at all grid points, independent of their blanking status.

Overset solvers typically employ a spatial smoothing operation to populate the solution within hole cuts with nonzero data as a fail-safe for inadvertent queries. Mavriplis et al. [16] outlined a general time-spectral solver for relative motion that leverages this feature. The process of solving Laplace's equation over the domain of blanked spatial nodes guarantees a complete solution time history at every mesh point, independent of its blanking status. The conventional time-spectral differentiation operator can then be applied to approximate the temporal derivative. Although attractive for its straightforward implementation, applying spatial smoothing proves inconsistent for the time-spectral method; nonphysical information provided by an alternative governing equation is propagated into the unblanked physical domain via the infinite support of the complex exponential basis functions. Although the resulting solution may be

smooth, it is dependent upon the arbitrary averaging of the solution through the blanked region. Blanked regions can be of any size and there is no expectation that a spatially smoothed solution in a blanked region will result in a Fourier expansion that successfully approximates the solution over the physically defined complement of the temporal interval. Consequently, spatial interpolation inhibits the desired temporal convergence with N [22]. Therefore, alternative strategies were pursued that avoid using arbitrarily filled data at the blanked nodes.

A natural approach to avoid corruption from unphysical data is to relinquish the global description of the solution by splitting the temporal domain into independent subperiodic intervals; time histories for dynamically blanked spatial nodes are partitioned into intervals of consecutively unblanked temporal collocation points. Independent temporal bases are used to represent the solution within each partition and differentiated accordingly. Global temporal support is thus abandoned at such nodes; however, this approach is consistent with the physics of disjoint domains separated by an impermeable boundary. This treatment does introduce a potential hazard for rapidly blanking nodes (i.e., if a node's status toggles between blanked and unblanked at every consecutive time instance, the solution will be considered constant in time at each of the active nodes, and consequently, the time derivative will be approximated as zero universally). Although this particular case may prove problematic, perhaps such situations warrant increased temporal resolution to resolve the high-frequency motion, suggesting incorporation of adaptive temporal refinement [23,24].

Several candidates were evaluated to determine an appropriate basis to represent the solution on bounded intervals of consecutively defined time samples. One option is to approximate derivatives using finite differences or a localized differentiable basis such as wavelets. However, compactly supported bases offer limited accuracy [25] and wavelet differentiation requires special treatment at nonperiodic interval boundaries [26]. Temporal extrapolation populates the undefined region using data only within the physical portion of the time signal, which can then be differentiated with the conventional Fourier-based operator. Examples of this approach, such as Fourier continuation, which extrapolates a nonperiodic function into a periodic function on a larger domain [27–29], and compressed sampling, which requires L_1 minimization to solve an underdetermined system [30], prove too costly or lack the requisite robustness for this application. Orthogonal polynomials (e.g., Chebyshev) can provide spectral accuracy on aperiodic domains, but demonstrate severe ill-conditioning on equidistant samples; approximation using orthogonal polynomials on equispaced data often exhibits violent oscillations on interval boundaries referred to as Runge's phenomenon [31]. Endpoint clustering resolves this issue but violates the prescribed constraint of uniform time sampling in the current application. A least-squares projection of orthogonal polynomials onto equispaced data is more stable, but results in an overdetermined system whose projection does not interpolate the solution data.

Barycentric rational interpolation (BRI) provides a viable alternative for overcoming the challenge of function approximation

on equispaced data [32]. Bos et al. [33] demonstrated their superior approximation and differentiation properties on equidistant nodes over conventional orthogonal polynomials. Efforts to explore rational interpolants and their utility as a pseudospectral basis for spectral collocation methods include but are not limited to [34–37]. In the approach ultimately adopted, solutions across each nonperiodic interval are expanded in a basis of rational interpolants and differentiated accordingly. Fully periodic intervals are still expanded and differentiated in the Fourier basis, resulting in a hybrid scheme.

Baltensperger et al. [38] define the rational interpolant $r(x)$, approximating the function f in barycentric form

$$r(x) = \frac{\sum_{k=0}^{N-1} (w_k / (x - x_k)) f(x_k)}{\sum_{k=0}^{N-1} (w_k / (x - x_k))} \quad (16)$$

and its corresponding differentiation operator \mathcal{D}_N , such that

$$\frac{d}{dx} r = \mathcal{D}_N r$$

$$d_k^j = \begin{cases} \frac{w_k / w_j}{(x_j - x_k)} & \text{if } j \neq k \\ -\sum_{\substack{i=0 \\ i \neq k}}^{N-1} d_i^j & \text{if } j = k \end{cases} \quad (17)$$

where $r(x_k) = f(x_k)$. The interpolation can be reformulated as a weighted sum of nodal basis functions $\phi_k(x)$, with coefficients equal to the nodal function values $f_k = f(x_k)$:

$$I_N f(x) = \sum_{k=0}^{N-1} f_k \phi_k(x), \quad \text{with } \phi_k(x) = \frac{(w_k / (x - x_k))}{\sum_{k=0}^{N-1} (w_k / (x - x_k))} \quad (18)$$

The barycentric rational basis functions nodally interpolate the solution data $\phi_k(x_j) = \delta_{jk}$, implying discrete orthogonality at the sample points.

Although similar in form to the Lagrange interpolant, a key distinction of the barycentric rational interpolant is in how the weights w_k are defined. The Lagrange interpolant is constrained to pass through $p + 1$ points as a polynomial of degree p . In contrast, although the rational interpolant passes through the data, it is not forced to do so as a polynomial of degree p . This relaxation helps alleviate spurious oscillations at the endpoints of equispaced nodes associated with the polynomial bases, while retaining powerful interpolation and differentiation properties.

Floater and Hormann [39] derived weights that provide an approximation order $d + 1$ while avoiding poles. The weights w_k control the accuracy and stability properties of the rational interpolant, which is a blend of polynomials of degree d . Weights guaranteeing an absence of poles are defined for N samples as

$$w_k = (-1)^{k-d} \sum_{i \in J_k} \prod_{j=i, j \neq k}^{i+d} \frac{1}{|x_k - x_j|} \quad (19)$$

where

$$I: = \{0, 1, \dots, (N-1) - d\} \quad \text{and} \quad J_\alpha: = \{i \in I: \alpha - d \leq i \leq \alpha\}$$

For uniform nodes, the resulting weights can be scaled to integer values without modifying the interpolant:

$$w_k = (-1)^{k-d} \sum_{i \in J_k} \binom{d}{k-i} \quad (20)$$

Readers are directed to the derivation by Floater and Hormann [39] for additional detail. Figure 3 illustrates three basis functions and

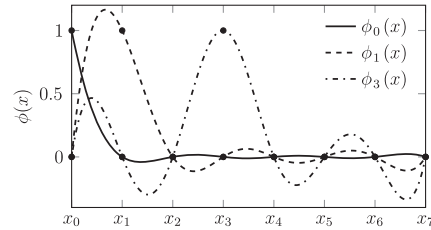


Fig. 3 Barycentric rational interpolant basis functions $\phi(x)$ corresponding to nodes $x_0, x_1,$ and x_3 using $d = 3$ over $N = 8$ equispaced nodes.

their respective nodal values, corresponding to the first, second, and fourth nodes, using $d = 3$ over eight equispaced sample points.

The application of barycentric rational interpolation to a representative signal taken from the inviscid plunging airfoil case in Sec. V is demonstrated in Fig. 4. In the first example, using nine global collocation points, shown in Fig. 4a, eight collocation points remain unblanked; note that the algorithm does not identify both interruptions in the continuous time signal because of the coarse sampling granularity that fails to place collocation points in each of the two continuous blanked regions. Thus, the solution spanning the eight unblanked nodes is expanded in a single basis. In the second example, depicted in Fig. 4b, 26 out of the 33 global collocation points remain unblanked. Employing the finer sampling of 33 global collocation points on the same representative signal results in two distinct intervals of dynamically blanked nodes that are each represented by independent barycentric rational interpolants. Interpolation error plots in Figs. 4c and 4d demonstrate excellent agreement with the continuous segments of the solution away from interval boundaries. It may be beneficial to detect the blanked region for the case using nine global collocation points, but this would require a potentially expensive preprocessor, using a fine sampling granularity to cycle through the motion and record the locations of all changes of blanking status.

Because the time-spectral method approximates temporal derivatives, the differentiation performance of each candidate must be assessed. The accuracy of rational interpolant-based differentiation is compared with finite differences, the Fourier differential operator (generally optimal for periodic functions), the Chebyshev differentiation operator on clustered Chebyshev nodes (generally optimal for nonperiodic functions), and differentiation operators derived from cubic splines with two different boundary conditions (natural and not-a-knot). An even-odd harmonic function $f(x) = 1 + \cos(\pi x) + \sin(\pi x)$ and Runge's function $f(x) = (1 + 25x^2)^{-1}$ are differentiated by a selection of the aforementioned methods. Convergence of differentiation error

$$\left\| \frac{df}{dx} - \mathcal{D}_N f \right\|_2$$

versus N is plotted in Fig. 5 for the harmonic function and Fig. 6 for Runge's function. The rational interpolant weight parameter

$$d = \min \left(\left\lfloor \frac{N-1}{2} \right\rfloor, d_{\max} \right)$$

is defined for different values of d_{\max} . The Fourier operator can theoretically differentiate the harmonic function exactly for $N \geq 3$, but exhibits roundoff error with increased N and demonstrates poor convergence for Runge's function. Chebyshev differentiation provides spectral convergence for both functions (albeit delayed for Runge's function in contrast to the harmonic function) and boundary condition selection makes a significant difference for spline-based differentiation. Although the rational interpolant-based differentiation operator demonstrates spectral-like convergence for $d_{\max} \in \{8, 16\}$ on the smooth harmonic function, it diverges for those values of d for small values of N in the case of Runge's function. Taking the best rational interpolant result for

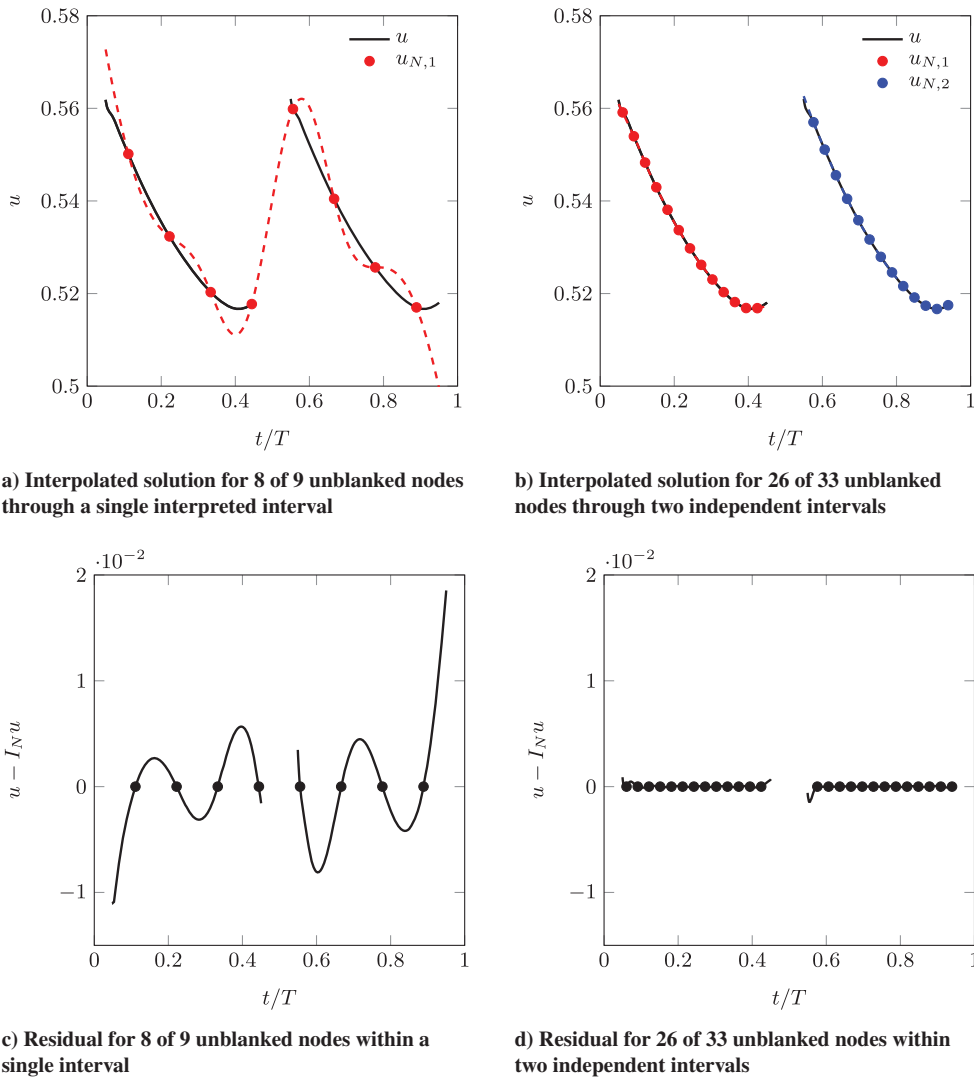


Fig. 4 Barycentric rational interpolation and residual $u - I_N u$ for $N = 9$ and $N = 33$ global collocation points with the default setting of $d_{\max} = 1$.

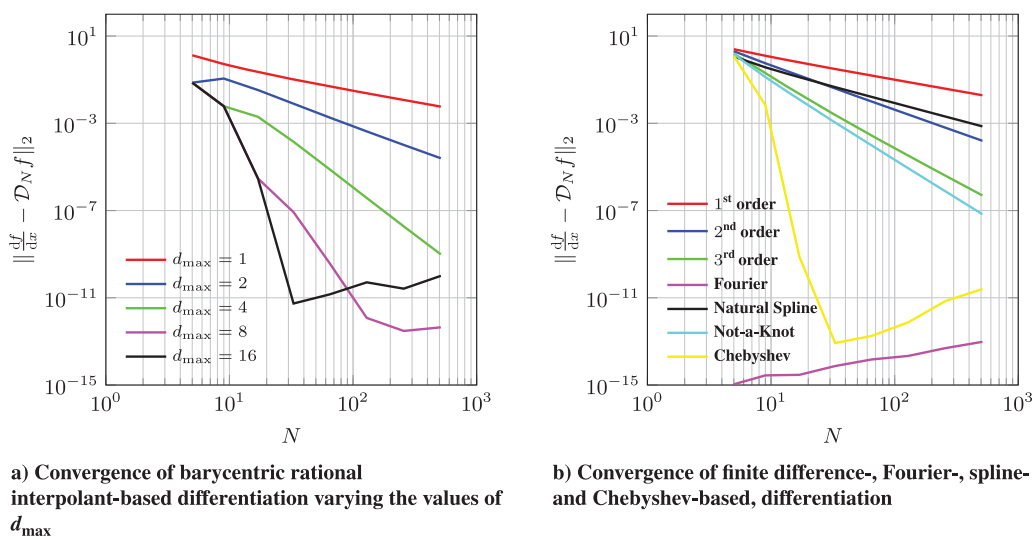


Fig. 5 Convergence of differentiated harmonic function $f(x) = 1 + \cos(\pi x) + \sin(\pi x)$, $x \in [-1, 1]$, using the barycentric rational interpolant-based differentiation operator for different values of d_{\max} and other differentiation operators.

every value of N in the Runge’s function example produces spectral-like convergence (even outperforming Chebyshev), reinforcing the importance of selecting an appropriate value for d . Using a lower value of d is associated with higher compactness and is therefore

more successful for high-frequency functions (e.g., Runge’s function) for small N . For smooth functions like the harmonic example, a large value of d poses no problem and the rational interpolant offers spectral-like approximation and differentiation

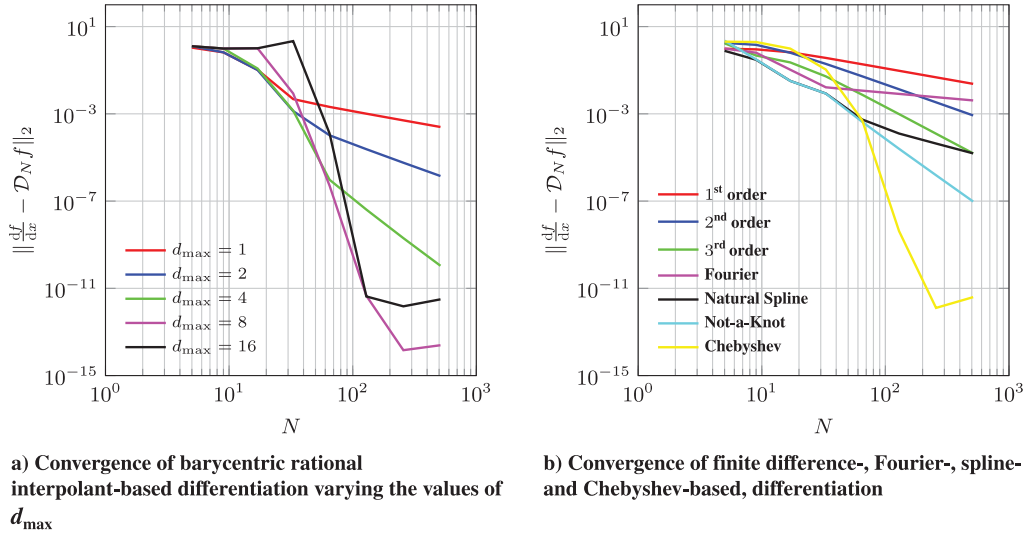


Fig. 6 Convergence of differentiated Runge's function $f(x) = 1/1 + 25x^2$, $x \in [-1,1]$, using the barycentric rational interpolant-based differentiation operator for different values of d_{\max} and other differentiation operators.

for large values of d_{\max} . Optimal selection of d is problem dependent and an area of ongoing research [36,40]; for robustness, a default value of $d_{\max} = 1$ was employed for the cases presented in Sec. V, unless otherwise noted.

The localized partitioned approach described earlier proved most successful in practice, but other representations were investigated and outlined by the first author [41]. These include a global expansion using a least-squares Fourier projection from all of the unblanked time samples at a dynamically blanked node and a mixed approach, where the aforementioned global expansion is augmented with a partitioned localized correction to recover an interpolation scheme.

IV. Implementation

The hybrid time-spectral scheme has been implemented within NASA's OVERFLOW code. OVERFLOW is an implicit finite difference-based RANS solver developed to handle a wide range of flow calculations on overset grids [42]. To avoid solving the global implicit system at every iteration, OVERFLOW employs an approximate-factorization scheme, whereby each dimension is solved sequentially. The approximate-factorization scheme [43] inverts a sequence of either block-tridiagonal or scalar-pentadiagonal operators, greatly reducing the computational effort required to update the solution at every iteration. An implicit time-spectral discretization can be incorporated within this framework by adding an additional factor in the temporal dimension.

OVERFLOW solves the unsteady Navier–Stokes equations in strong conservation-law form:

$$\frac{\partial Q}{\partial t} + \nabla \cdot \mathbf{F}(Q) \quad (21)$$

Flux components $\mathbf{F} = \{F, G, H\}^T$ in the x , y , and z directions, respectively, are nonlinear functions of the state vector of conserved quantities of mass, momentum, and energy, $Q = \{\rho, \rho u, e\}^T$, which are composed of both convective and viscous constituents. The equations are presented here in Cartesian coordinates but are solved in generalized curvilinear coordinates.

OVERFLOW is equipped with both steady-state and TA modes, but because only unsteady problems are considered, the time-accurate scheme will be briefly outlined and followed by a description of the TS discretization and implementation.

A. Time-Accurate Scheme

A dual time-stepping scheme [44] is applied for the general case of time-dependent flow. A physical time step size is selected to provide the desired level of time accuracy and the unsteady residual is

sufficiently reduced at each step as the solution is marched forward in time. The time derivative of the state vector of conserved quantities is approximated using the second-order backward difference formula (BDF2):

$$\frac{3Q^{n+1} - 4Q^n + Q^{n-1}}{2\Delta t} + \delta_x F^{n+1} + \delta_y G^{n+1} + \delta_z H^{n+1} = 0 \quad (22)$$

The spatial finite difference operators δ_x , δ_y , and δ_z are applied to the corresponding flux vectors in the x , y , and z directions, respectively. The dual time-advancement scheme is achieved by adding a pseudotime continuation discretized by the first-order backward Euler scheme, with subiteration index s :

$$\frac{Q^{s+1} - Q^s}{\Delta \tau} + \frac{3Q^{s+1} - 4Q^s + Q^{s-1}}{2\Delta t} + \delta_x F^{s+1} + \delta_y G^{s+1} + \delta_z H^{s+1} = 0 \quad (23)$$

Because the flux vectors are nonlinear functions in Q , they are linearized about Q^s . The linearizations are substituted into Eq. (23), which is then put into delta form, where A , B , and C are the flux Jacobians in the x , y , and z directions, respectively,

$$\Delta \tilde{\tau} = \frac{\Delta \tau}{1 + (3\Delta \tau / 2\Delta t)}$$

and $\Delta Q = Q^{s+1} - Q^s$:

$$[I + \Delta \tilde{\tau} \delta_x A + \Delta \tilde{\tau} \delta_y B + \Delta \tilde{\tau} \delta_z C] \Delta Q = -\Delta \tilde{\tau} \left[\frac{3Q^s - 4Q^n + Q^{n-1}}{2\Delta t} + \delta_x F^s + \delta_y G^s + \delta_z H^s \right] \quad (24)$$

An approximate factorization of the left-hand side (LHS) of Eq. (24) results in the final form of the system of equations, where $\mathbf{R}(Q^s)$ is the right-hand side (RHS) of Eq. (24):

$$[I + \Delta \tilde{\tau} \delta_x A][I + \Delta \tilde{\tau} \delta_y B][I + \Delta \tilde{\tau} \delta_z C] \Delta Q = \mathbf{R}(Q^s) \quad (25)$$

The solution is updated by applying a sequence of low-rank inversions onto the RHS of Eq. (25) on a point-by-point basis. This second-order accurate dual time-stepping procedure is used for the time-accurate calculations presented in Sec. V.

B. Time-Spectral Scheme

The OVERFLOW time-spectral implementation is introduced as a modification to the discretization of the time derivative in Eq. (22), where an infinitely supported, spectrally accurate temporal differentiation operator replaces an algebraically accurate finite difference approximation:

$$\sum_{j=0}^{N-1} d_j^n Q^{j,s+1} + \delta_x F^{n,s+1} + \delta_y G^{n,s+1} + \delta_z H^{n,s+1} = 0 \quad (26)$$

Equation (26) holds for all time samples $n \in \{0, \dots, N-1\}$, and the solution array $Q^{n,s}$ corresponds to the s th iteration of the n th time sample; the same notation holds for the flux vectors. As with the time-accurate case, a backward Euler pseudotime continuation augments Eq. (26):

$$\frac{\Delta Q^n}{\Delta \tau} + \sum_{j=0}^{N-1} d_j^n Q^{j,s+1} + \delta_x F^{n,s+1} + \delta_y G^{n,s+1} + \delta_z H^{n,s+1} = 0 \quad (27)$$

Linearizations of the flux vectors about $Q^{n,s}$ are substituted into Eq. (27), which is then put into delta form where A and B are the same flux Jacobians described for the time-accurate scheme:

$$\begin{aligned} \frac{\Delta Q^n}{\Delta \tau} + \sum_{j=0}^{N-1} d_j^n \Delta Q^j + [\delta_x A + \delta_y B + \delta_z C] \Delta Q^n \\ = - \left[\sum_{j=0}^{N-1} d_j^n Q^{j,s} + \delta_x F^{n,s} + \delta_y G^{n,s} + \delta_z H^{n,s} \right] \end{aligned} \quad (28)$$

We can express Eq. (28) over the complete space–time domain, where

$$\begin{aligned} \Delta Q &= \{\Delta Q^0, \dots, \Delta Q^{N-1}\} \\ \mathbf{R}(Q) &= \{\mathbf{R}(Q^0), \dots, \mathbf{R}(Q^{N-1})\} \end{aligned}$$

are arrays of the update and spatial residual, respectively, over both space and time. The global temporal differentiation operator D_N is constructed via permutations of the local temporal differentiation operator \mathcal{D}_N and \tilde{A} , \tilde{B} , and \tilde{C} are block diagonal spatial Jacobian operators applied over all N time instances,

$$\left[I + \Delta \tau D_N + \Delta \tau \delta_x \tilde{A} + \Delta \tau \delta_y \tilde{B} + \Delta \tau \delta_z \tilde{C} \right] \Delta Q = \mathcal{R}(Q^s) \quad (29)$$

where $\mathcal{R}(Q^s) = -\Delta \tau [D_N Q^s + \mathbf{R}(Q^s)]$. Finally, the LHS of Eq. (29) is approximately factored, treating time as an additional direction:

$$[I + \Delta \tau \delta_x \tilde{A}] [I + \Delta \tau \delta_y \tilde{B}] [I + \Delta \tau \delta_z \tilde{C}] [I + \Delta \tau D_N] \Delta Q = \mathcal{R}(Q^s) \quad (30)$$

The solution is updated by applying a sequence of $N_{SD} + 1$ directional inversions onto the RHS of Eq. (30) $\mathcal{R}(Q^s)$. The initial updates are performed in the N_{SD} spatial dimensions for each time sample j and the final inversion is performed in the temporal dimension at every point in space, indexed by i , using the dense local temporal differentiation operator

$$\begin{aligned} [I + \Delta \tau \delta_x A] \Delta \hat{Q}^j &= \mathcal{R}(Q^{j,s}) \\ [I + \Delta \tau \delta_y B] \Delta \bar{Q}^j &= \Delta \hat{Q}^j \\ [I + \Delta \tau \delta_z C] \Delta \bar{\bar{Q}}^j &= \Delta \bar{Q}^j \\ [I + \Delta \tau D_N] \Delta Q_i &= \Delta \bar{\bar{\bar{Q}}}_i \end{aligned}$$

The required modifications to the existing solver are limited to an additional linear solve of, at most, dimension N , at every grid point for the implicit temporal operator and an evaluation of the

temporal derivative at every grid point (a matrix–vector product of dimension N). In other words, time is treated in a similar fashion to the spatial independent variables when solving for the steady-state solution in the combined space–time domain.

For spatial nodes equipped with complete time histories, the standard Fourier-based differentiation operator is used for \mathcal{D}_N . However, for dynamically blanked nodes, \mathcal{D}_N derived from a rational interpolant of dimension $N_P < N$ is dynamically generated and used for the intervals of N_P consecutively defined time samples. For statically blanked (Fourier-based) nodes, the approximately factored time-spectral implicit temporal operator $[I + \Delta \tau \mathcal{D}_N]$ can be diagonalized by the discrete Fourier transform if $\Delta \tau$ is held constant for each time sample ($\Delta \tau$ is still free to vary in space to enable local pseudotime stepping). Thus, the temporal update at statically blanked nodes is reduced from an implicit linear system of equations to a series of scalar equations, removing the need to invert a dense LHS operator. Using the fast Fourier transform (FFT) to evaluate the temporal derivative and diagonalize the implicit system reduces the complexity from $\mathcal{O}(N^3)$ to $\mathcal{O}(N \log N)$ matching the explicit nonlinear frequency domain method [45]:

$$\begin{aligned} \tilde{R}_k &\leftarrow \text{FFT}(\Delta \bar{\bar{\bar{Q}}}_i) \\ \Delta \tilde{Q}_k &\leftarrow \tilde{R}_k / (1 + \Delta \tau i \omega k), \quad \forall k \\ \Delta Q_i &\leftarrow \text{IFFT}(\Delta \tilde{Q}) \end{aligned}$$

where the inverse fast Fourier transform is denoted as IFFT.

The time-spectral approach as applied to OVERFLOW avoids modifying the existing spatial residual and implicit operators because they are applied to each time sample sequentially within each iteration. All of the cases presented employ second-order finite differences, with second- and fourth-difference artificial dissipation using OVERFLOW's default settings of $\epsilon_2 = 2.0$ and $\epsilon_4 = 0.04$ dissipation coefficients. The primary convergence acceleration technique employed by OVERFLOW is the FAS multigrid algorithm. The FAS spatial multigrid scheme was augmented to include the fully implicit time-spectral discretization on all grid levels. The time-spectral multigrid implementation has demonstrated a multifold increase in computational efficiency [41].

Naturally, there are both memory and computational overheads associated with a time-spectral calculation above the costs associated with an analogous steady-state computation. The extra cost is offset by the capability of converging to a space–time solution more rapidly than a time-accurate calculation. The efficiency merits of Fourier pseudospectral methods have been demonstrated in great detail by McMullen [4,45], among others. The costs specific to the current implementation will be described, however, timings of time-spectral calculations are not provided because the augmented code has not been fully optimized.

Complete space–time solution and residual arrays must be stored for each of the N time samples. If N_x is the number of spatial nodes and N_Q is the number of solution variables, then the total memory for the global solution and residual arrays are each $N \times (N_x \times N_Q)$. A metric array of size $13N_x$ (in three spatial dimensions) and an integer array of N_x blanking values are also stored for each of the N time samples. For example, a computation involving 125 million grid points distributed across 50 20-core Ivy Bridge nodes, each equipped with 64 GB of memory, can employ upward of 100 time samples, which is beyond what is typically used in practice. A low-storage option can be used when memory is limited, where the metric and blanking arrays are reevaluated every iteration. Although this suggests that a large number of temporal modes can be applied without risk of exhausting the memory budget on suitably parallelized calculations, there is also an opportunity to introduce a second level of parallelization by distributing the time samples onto different processors. This parallel space–time time-spectral strategy was first demonstrated by Mavriplis and Yang [18].

The primary computational overhead resulting from the implicit approximately factored time-spectral solver is attributable to the evaluation of the temporal derivative approximation (RHS) and the linear solve in the temporal dimension (LHS) at every mesh point.

As previously mentioned, the $\mathcal{O}(N \log N)$ FFT/IFFT can dramatically reduce the computational cost of both the temporal derivative evaluation and the linear solve. The FFT cannot be leveraged at dynamically blanked nodes and therefore such nodes require a matrix–vector product and a dense linear solve; however, the number of dynamically blanked nodes is generally a small fraction of the overall number of spatial degrees of freedom. The matrix–vector products and linear solves can also be executed for the Fourier-based nodes, but the savings afforded by the FFT become quite significant for even a modest number of temporal degrees of freedom.

V. Numerical Results

Numerical experiments in both two and three spatial dimensions are presented to demonstrate the ability of the proposed hybrid time-spectral scheme to accurately resolve cases involving relative motion within an overset framework. Results computed with the time-spectral discretization are compared with reference solutions of highly resolved time-accurate calculations. Computational efficiency of the time-spectral implementation is not explicitly addressed; the literature provides strong support for Fourier collocation schemes due to their potential to dramatically reduce execution times required to compute periodic steady-state flows in comparison with traditional time-marching schemes; the proposed scheme does not inhibit this expected performance but expands the range of cases that can be tackled with the time-spectral methods by including relative motion for overlapping meshes.

The section begins with a subsonic inviscid plunging airfoil test case; a large plunge amplitude exposes a substantial number of dynamically blanked nodes that are swept out by the airfoil over the course of the oscillation. Next, inviscid and turbulent RANS transonic pitching airfoil cases corresponding to the AGARD 702 CT5 experiment [46] are used to assess the capability of the time-spectral scheme to resolve dynamic shocks and turbulent wakes. Finally, three-dimensional calculations of the quarter-scale V-22 rotor are presented for both hover and forward (edgewise) flight. In most cases, results for both rigid and relative motion were computed using the OVERFLOW time-spectral implementation, providing a direct comparison between the standard time-marching scheme, the conventional time-spectral method, and the proposed hybrid strategy.

A. Large-Amplitude Inviscid Plunging Airfoils

A large-amplitude inviscid plunging NACA 0012 airfoil test case provides a meaningful demonstration of the hybrid time-spectral scheme because the motion introduces a significant number of dynamically blanked nodes. This section first examines the accuracy of the barycentric rational interpolant representation discussed in Sec. III by evaluating how closely the time-spectral solution approximates the time-accurate solution at a dynamically blanked sensor node. Modal convergence in the drag coefficient is then demonstrated for both the rigid- and relative-motion cases.

The instantaneous vertical displacement $y(t) = h \sin(kt)$ is defined as a single sinusoid of the reduced frequency $k = \omega c / V_\infty$. The plunge amplitude is selected as half the chord length, resulting in a nondimensional plunge amplitude $h = a/c = 0.5$, with a reduced frequency of $k = 0.1627$ rad per nondimensional time unit, corresponding to the AGARD 702 [46] case that follows. The freestream Mach number $M_\infty = 0.5$ maintains subsonic flow throughout the domain. A near-body O mesh with 241×30 points in the chordwise and body-normal directions, respectively, is embedded within a 341×261 rectilinear off-body grid that stretches approximately $100c$ to the far-field boundaries in both the x and y directions. A sensor node is placed on the Cartesian grid at the midchord position ($x = 0.5c$) of the neutral axis of oscillation ($y = 0$) because this y location experiences the maximum instantaneous plunge velocity.

Figure 7 tracks the time history of streamwise momentum at the dynamically blanked sensor node and compares results using barycentric rational interpolants, a least-squares Fourier projection, and the spatial smoothing approach. Streamwise momentum ρu is used to assess the performance of each scheme because it is the most

sensitive of the conserved quantities. The airfoil initially blanks the sensor node as it moves upward, blanks it again on its downward stroke, and once again as the airfoil completes its cycle. Accuracy is evaluated by computing the rms error of the time-spectral versus time-accurate solution at the unblanked collocation points. Solutions computed using barycentric rational interpolants are shown in Fig. 7a and compared against the use of the globally expanded least-squares (LS) Fourier projection in Fig. 7b and the spatial smoothing approach in Fig. 7c. The three methods all perform similarly for the cases of three and five global collocation points, but the rational interpolants demonstrates better agreement for the cases using additional global time samples. For the case of 33 global time samples, both of the Fourier expansions exhibit high-frequency oscillations, whereas the result computed using two independent partitioned segments spanned by barycentric rational interpolants demonstrates no such oscillations (in the scale of the figure). The superior convergence of the bounded interval approach is confirmed in Fig. 7d, where three choices of d_{\max} are presented for the barycentric rational interpolant in addition to the spatial smoothing approach and the global least-squares approach; a constant zero-derivative result is plotted as a reference. Although this analysis is presented for a single representative node, the results demonstrate the general behavior observed at all of the sensor nodes surveyed to date. For the remainder of the discussion, the default treatment for dynamically blanked nodes is barycentric rational interpolation using $d_{\max} = 1$.

The previous analysis examined the accuracy of the hybrid time-spectral approach at a particular dynamically blanked grid point. However, design is often driven by functionals of integrated scalar performance measures, such as lift and drag. Drag coefficient polars are therefore used to evaluate how well the time-spectral solutions match the time-accurate result. The time-spectral solutions are interpolated from their collocation points to reconstruct a continuous signal over the period. Continuous time histories of force and moment coefficients are then evaluated from these synthesized solutions and compared with the time-accurate signals.

Figure 8 plots the time-accurate sectional drag coefficient c_d versus vertical displacement h over the period against the time-spectral results for $N \in \{3, 9, 33\}$. The time-accurate calculation is initialized with a steady-state solution and simulated for 10 periods of oscillation; the drag signal settles into a periodic steady state relatively quickly. For the case of three time samples, depicted in Fig. 8a, neither the conventional time-spectral method nor the hybrid time-spectral method accurately match the drag coefficient signal generated using the time-marching scheme. However, solution values at the collocation points strongly agree with the time-accurate result, especially for the rigid-motion case using the standard time-spectral method. As the temporal resolution is refined to nine samples, as depicted in Fig. 8b, both the rigid- and relative-motion interpolated signals demonstrate strong agreement with the time-accurate signal, although slight discrepancies between the standard and hybrid time-spectral methods remain. Finally, for the case using 33 time samples, depicted in Fig. 8c, the two time-spectral methods demonstrate near complete agreement with each other and the time-accurate scheme.

Monotonic convergence of both the standard (Fig. 9a) and hybrid (Fig. 9b) time-spectral calculations are demonstrated in Fig. 9 by plotting the continuous drag coefficient signals for $N \in \{3, 5, 9, 17, 33\}$ versus the periodic steady-state time-accurate signal. For the case of rigid motion using the standard time-spectral method, the signal computed using two harmonics ($N = 5$) nearly matches the time-accurate result. However, the hybrid scheme for the relative motion case requires four to eight harmonics to achieve similar agreement with the time-accurate signal. Thus, for this case, the use of relative motion requires additional modes beyond those required using rigid motion to achieve qualitative agreement with the time-accurate result.

This case has demonstrated the ability of the proposed hybrid time-spectral scheme to successfully predict the performance of a plunging airfoil that moves relative to a stationary background grid. However, the convergence of the relative-motion time-spectral scheme lags behind its rigid-motion counterpart. The suboptimal basis functions used to approximate the solution at dynamically blanked nodes

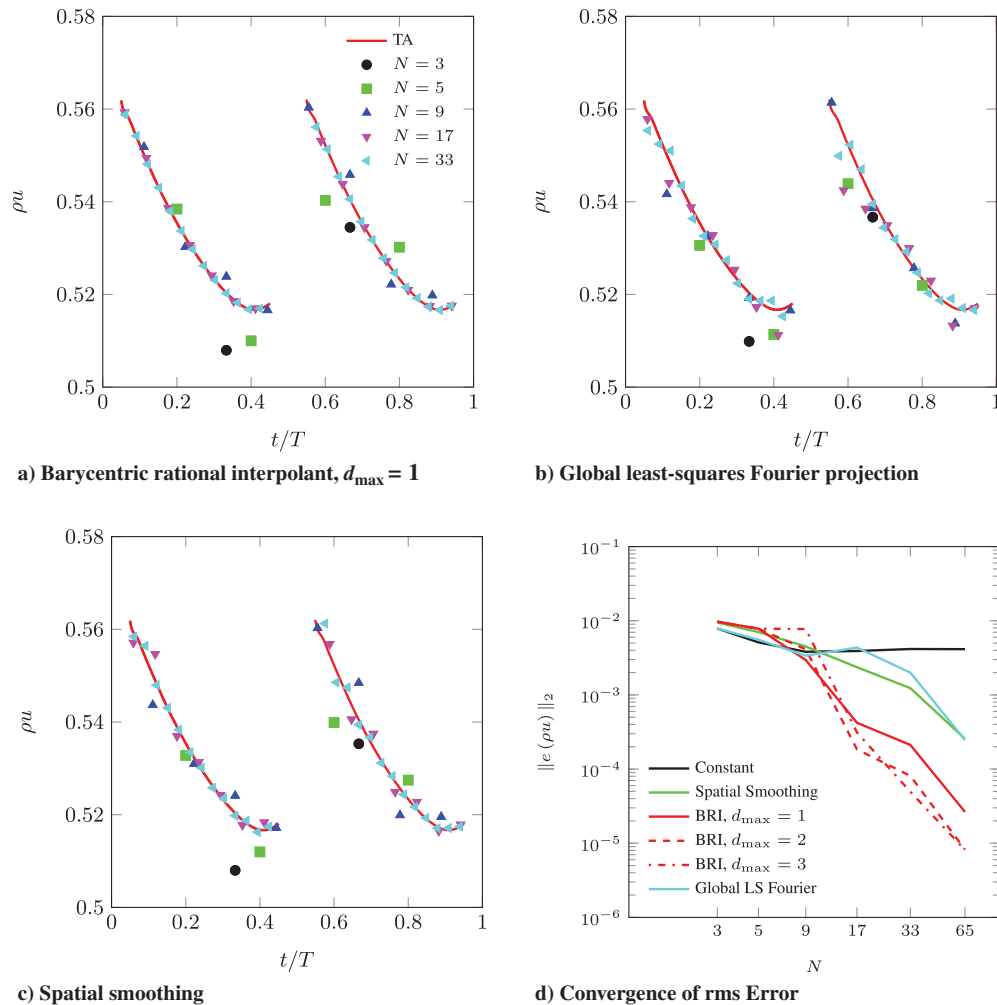


Fig. 7 Time-spectral vs time-accurate values of streamwise momentum at the sensor node.

assumes partial responsibility, but the fact that the stationary background grid is not moving with the body is also to blame; the solution on the background grid remains periodic, however, its frequency content is augmented by the relative motion between itself and the plunging near-body grid. Consider the solution at a point on the near-body grid moving with the airfoil. Over the course of the period of motion, it experiences smooth transitions between compressions and expansions. Although a stationary point on the background grid in the vicinity of the airfoil experiences periodic compressions and expansions, the transitions become more rapid as the plunge amplitude increases; the airfoil moves past the stationary point with a larger velocity and therefore the transition occurs over a shorter duration. This increases the frequency of the response that needs to be approximated by the discrete Fourier series. Therefore, for a given plunge amplitude and reduced frequency, more modes must be retained to resolve the relative-motion case because its solution contains higher harmonics on the stationary background grid compared with the solution on the moving background grid of the rigid motion case.

Figures 10 and 11 provide the time- and frequency-response, respectively, of the subsonic inviscid plunging airfoil at a node located approximately $0.35c$ downstream of the trailing edge on both the near- and off-body grids in the neutral position of the oscillation ($y = 0$). For the case of rigid-body motion, the off-body grid translates with the near-body grid and the nodes remain approximately coincident for all time. For the case of relative motion, the node on the off-body grid remains in place and is therefore only approximately coincident with the node on the near-body grid at two times over the period of oscillation. The higher-frequency content in the solution at a node on the stationary

background grid suggests that more frequencies are required to resolve the solution using relative motion than with rigid motion. Figure 12 supports this assertion by plotting the reconstruction of the off-body grid solution from the frequency components defined by a discrete Fourier transform of the time-accurate solution. Figure 12a demonstrates that roughly four modes are sufficient to adequately resolve the solution at the off-body grid point for the case of rigid-body motion. However, the reconstructions plotted in Fig. 12b suggest that 30 or more modes are required to sufficiently resolve the flow at the stationary off-body grid point. However, many fewer modes are required to match the time-accurate result with respect to integrated loads such as drag (Fig. 9), supporting the time-spectral method as a potential reduced-order model. For such simple cases, rigid motion would naturally be a more efficient choice because fewer modes are required to resolve the flow. However, more complex configurations require relative motion for nondeforming grids.

B. Transonic Pitching NACA 0012 Airfoil

The time-spectral formulation is next compared with time-accurate simulations and experimental data corresponding to the AGARD 702 CT5 oscillatory pitch test case [46]. Both inviscid and viscous turbulent simulations are performed on this transonic $M_\infty = 0.755$ case. The airfoil pitches about its quarter-chord with incidence $\alpha(t) = \alpha_0 + \alpha \sin(kt)$. This case employs mean incidence, $\alpha_0 = 0.016$ deg and pitch amplitude $\alpha = 2.51$ deg, with reduced frequency $k = 0.1627$ rad per nondimensional time unit.

A hierarchy of time-spectral simulations have been computed using an increasing number of time samples to investigate the performance of the scheme with increased temporal resolution. The near-body grid and its overlap region are chosen such that the

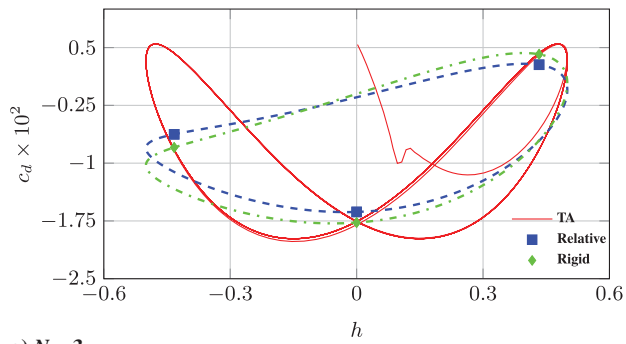
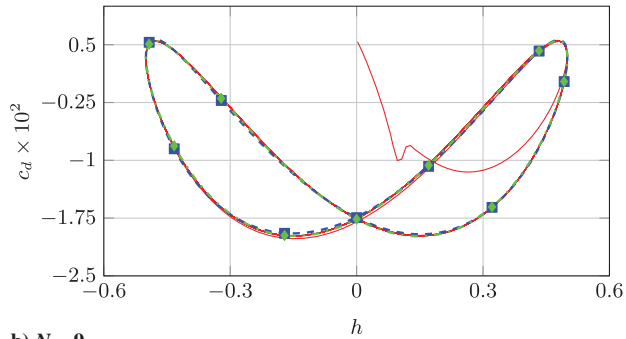
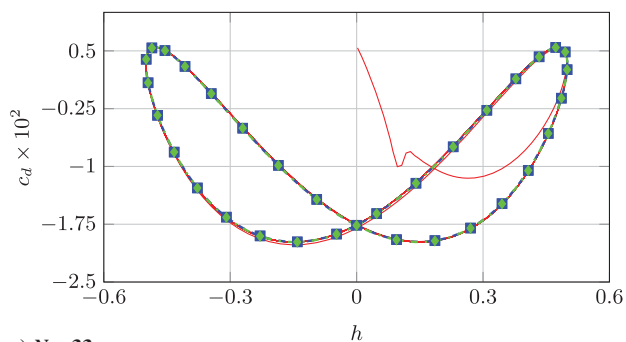
a) $N = 3$ b) $N = 9$ c) $N = 33$

Fig. 8 Time-spectral vs time-accurate drag coefficients for $N \in \{3, 9, 33\}$ for rigid and relative motion.

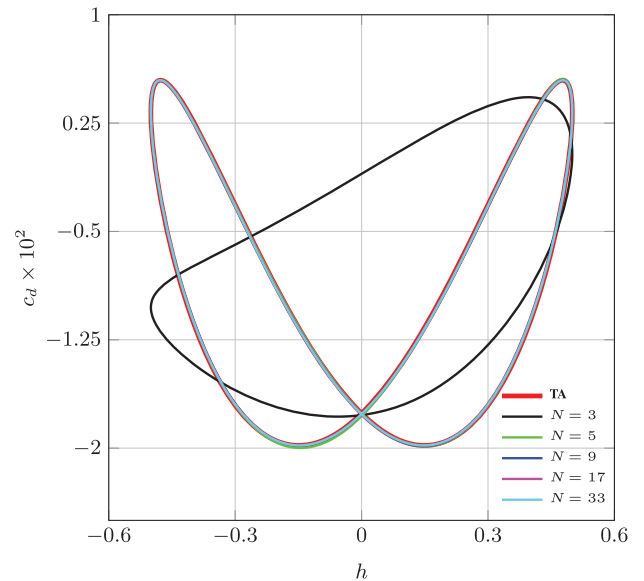
transient shock spans the grid interface. Figure 13 shows the supersonic region for both the inviscid (Fig. 13a) and viscous (Fig. 13b) grid systems at time $t = T/N$ for the $N = 5$ case.

1. Inviscid Case

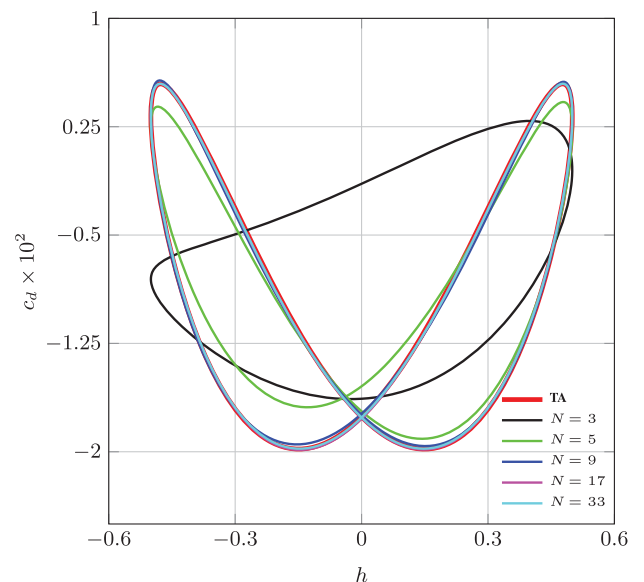
A near-body O mesh with 241×30 points in the chordwise and body-normal directions, respectively, is embedded within a 341×261 Cartesian background grid that stretches approximately $100c$ to the far-field boundaries in both directions (Fig. 13a). Pitching moment and drag coefficient polars are plotted in Figs. 14 and 15, respectively. The rigid- and relative-motion time-spectral solutions converge to nearly the same solution computed with the time-accurate scheme. Reasonable agreement with the experimental data is achieved, but most important, monotonic convergence of the hybrid time-spectral solutions is achieved by increasing the number of time samples. A resolution of 33 time samples is sufficient for both the relative- and rigid-body time-spectral calculations to match the time-accurate pitching moment signal, but a modest number of additional time samples are needed to fully resolve the kink in the drag signal at $\alpha \approx \pm 2$ deg.

2. Turbulent Reynolds-Averaged Navier–Stokes Case

Practical applications of the time-spectral method, including rotorcraft and turbomachinery, involve turbulent flows, and therefore



a) Rigid Motion



b) Relative Motion

Fig. 9 Convergence of rigid- and relative-motion time-spectral drag coefficient signals to the periodic steady-state time-accurate calculation.

the previous oscillatory airfoil test case is extended to use the Spalart–Allmaras one-equation turbulence model on a viscous grid system. A near-body C mesh with 241×84 points in the chordwise and body-normal directions, respectively, is embedded within a 875×375 Cartesian background grid that stretches approximately $100c$ to the far-field boundaries in both directions (Fig. 13b). The time-spectral implementation employs a semi-implicit turbulent update, as described in [22], to avoid a massive overhaul of the codebase.

To illustrate a potential difficulty of applying the time-spectral method to the positivity-constrained one-equation Spalart–Allmaras turbulence model, consider Fig. 16, showing contours of the (undamped) turbulent eddy viscosity $\tilde{\nu}$ in the wake region at five temporal collocation points over the period of oscillation. These images demonstrate the potentially large changes in $\tilde{\nu}$ as a function of time at a particular point in the wake. Figure 17 plots the time history of turbulent eddy viscosity and its temporal derivative at one such point downstream of the airfoil, through which the turbulent wake passes during a portion of the oscillation. Note that, in Fig. 17a, the turbulent eddy viscosity transitions from a constant value $\mathcal{O}(1)$ to a large value $\mathcal{O}(1000)$ and back over a small fraction of the period.

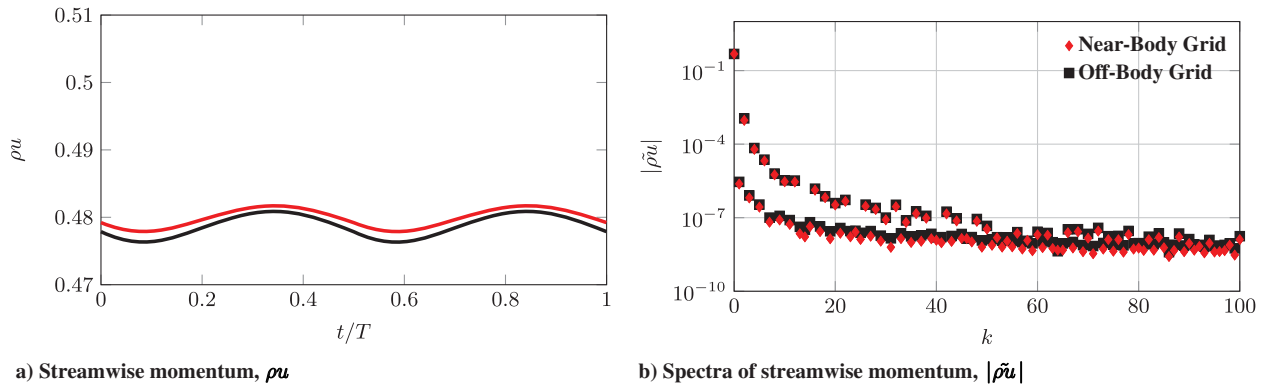


Fig. 10 Time and frequency response of a plunging airfoil with an off-body grid translating with the airfoil (rigid motion).

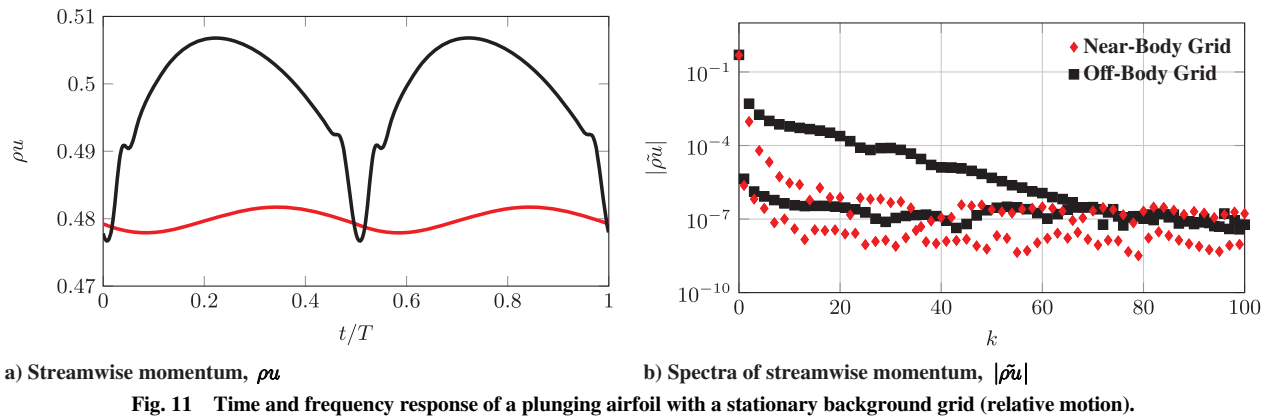


Fig. 11 Time and frequency response of a plunging airfoil with a stationary background grid (relative motion).

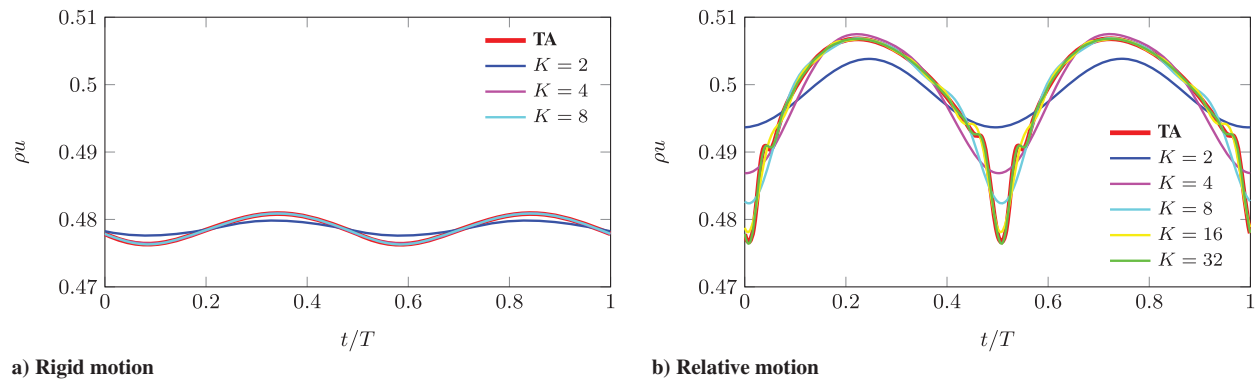
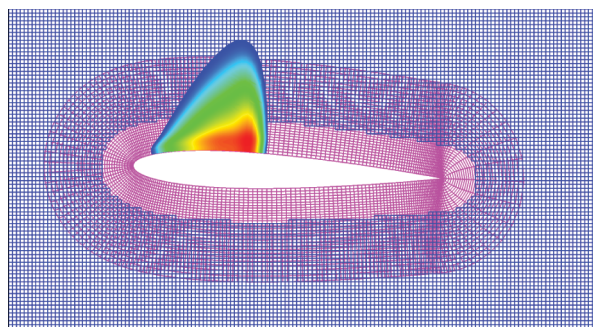


Fig. 12 Reconstruction of streamwise momentum using K modes at a node on the off-body grid a) translating with the airfoil and b) stationary relative to the translating airfoil.

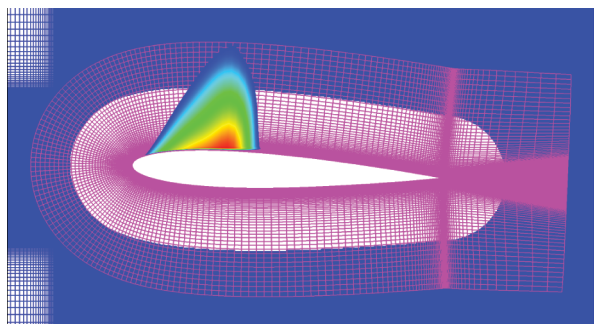
Although the function varies smoothly in the context of the small physical time step employed for a time-accurate calculation, it resembles a discontinuous step function in the frame of the much coarser resolution of time-spectral collocation points, leading to spurious oscillations in the Fourier expansion. Oscillations in the gradient are manifested at the discrete sample points that can be observed in Fig. 17b, resulting in large overshoots. This issue is compounded by the fact that undamped eddy viscosity remains close to zero outside the wake, so that modest overshoots in the derivative may violate the positivity constraint on $\tilde{\nu}$. The current example uses eddy viscosity in the Spalart–Allmaras model, however, similar issues are encountered for turbulent kinetic energy or dissipation in other models. The same phenomenon could also manifest itself in the fluid equations for high-speed cases. Note that this issue applies to time-spectral treatment of turbulence in general as it occurs downstream from the body on nodes equipped with complete time histories. Applying a limiter to the temporal differentiation operator maintains positivity on $\tilde{\nu}$ without sacrificing accuracy. The current

limiter sets the time-spectral temporal residual to zero if it is estimated to drive $\tilde{\nu}$ negative. Figure 17a demonstrates good agreement between the time-spectral and time-accurate solutions for $\tilde{\nu}$ at the collocation points despite application of the limiter. Slight ringing does occur in the constant region but the turbulent eddy viscosity remains positive.

Only the relative-motion time-spectral scheme is applied to the viscous case because the hybrid scheme already demonstrated its ability to match the results computed with the conventional time-spectral scheme for the inviscid rigid-body case. The pitching moment and drag coefficients extracted from the time-spectral solutions converge to those computed in unsteady mode with increasing temporal collocation points (Figs. 18 and 19). As with the inviscid example, the case employing 33 time samples demonstrates near-exact agreement with the time-accurate pitching moment signal, but fully resolving the kink in the drag coefficient signal at $\alpha \approx \pm 2$ deg (Figs. 18c and 19c) would require additional modes. Less agreement is observed with the experimental data in the pitching



a) Inviscid



b) Turbulent RANS

Fig. 13 Grid system and supersonic regions for both the a) inviscid O mesh and b) turbulent RANS C mesh at time $t = T/N$ for the $N = 5$ case.

moment coefficient polars (Fig. 18) when compared with the inviscid case from the previous section, but this discrepancy also occurs in the time-accurate result, suggesting a physical modeling issue. Although experimental data are included for reference, the crucial point remains that the time-spectral results converge monotonically to those computed with the time-accurate solver.

C. Isolated V-22 Tiltrotor

The present section assesses the ability of the proposed time-spectral approach to successfully match time-accurate predictions of a realistic three-dimensional application: the isolated V-22 rotor. Selecting the V-22 rotor with its stiff and relatively low-aspect-ratio blades permits the simplifying assumption of nondeforming geometry, removing the need to account for aeroelasticity. Additionally, the V-22 rotor is not typically employed in forward (edgewise) flight because it operates in either hover mode or airplane (propeller) mode. Nevertheless, forward-flight time-spectral results are compared with those computed in an unsteady environment to evaluate the predictive capabilities of the proposed scheme for the flight regime that often introduces relative motion in an overset simulation.

1. Hover

The V-22 rotor system has been analyzed extensively for hover, both experimentally and numerically. The quarter-scale TRAM was tested at the Duits-Nederlandse wind tunnel [47,48]. The isolated rotor geometry is used for all calculations presented, which is consistent with the numerical experiments detailed in [49–52].

The typical overset solution procedure involves revolving the body-fitted curvilinear grids through a system of stationary background grids. Despite the relatively low aspect ratio of the V-22 blades, a successful time-spectral simulation using this approach would require retaining a large number of harmonics due to the high-frequency response induced on the fixed background grids by the relatively low-frequency signals on the near-body grids moving with the blades; this observation is analogous to the two-dimensional plunging airfoil result shown in Fig. 11 where a relatively low-frequency signal on moving near-body grids induces a much

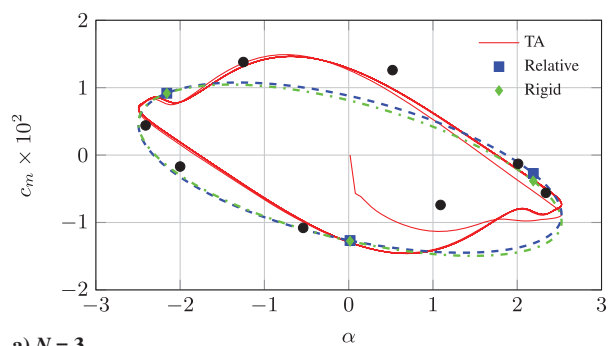
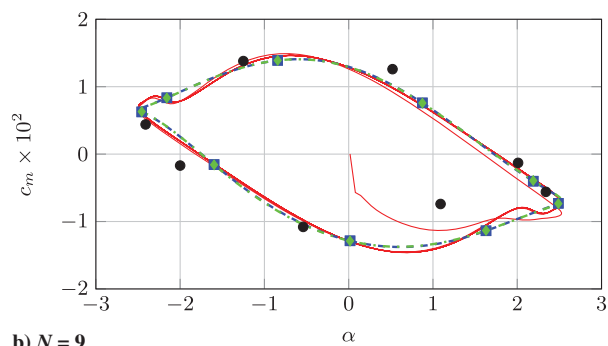
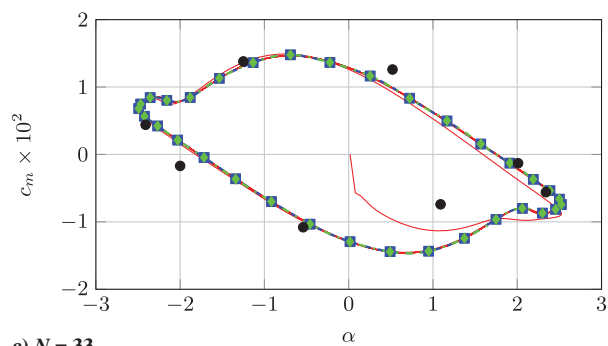
a) $N = 3$ b) $N = 9$ c) $N = 33$

Fig. 14 Time-spectral vs time-accurate pitching-moment coefficients for $N \in \{3, 9, 33\}$ for rigid and relative motion. Experimental data from the AGARD 702 report [46] are plotted with black dots.

higher-frequency response on stationary background grids. Alternatively, rigid-body motion can be achieved by rotating the background grids with the blades. Because hover can be well estimated as a steady flow in the rotating frame,[§] we expect using only a single mode will adequately resolve the flow when all grids rotate in unison. However, this configuration fails to introduce any dynamically blanked nodes and therefore the hover case is used to validate the three-dimensional OVERFLOW time-spectral implementation; dynamically blanked nodes are introduced in the forward-flight case that follows.

The grid system includes three blades, each composed of a C-mesh blade grid and two cap grids, one each for the root and tip. The C mesh consists of $181 \times 94 \times 65$ points in the chordwise, radial, and body-normal directions, respectively. Each blade, root, and tip grid contains 1.1, 0.48, and 0.33 million grid points, respectively, for a total of 5.7 million near-body grid points. The off-body grid system consists of a hierarchy of 46 isotropic Cartesian grids spanning 15 rotor radii R to the far-field boundaries in each direction, resulting in 21.3 million off-body mesh points, for a total of 27.1 million grid points overall. The finest Cartesian (level-one or L1) grid spans roughly $\pm 1.2R$ in both the x and y directions and $-1.9R$ and $+0.38R$ in the z direction, with spacing of $0.1c_{\text{tip}}$. Although a centerbody is

[§]See Potsdam and Strawn [49] for noninertial reference frame results.

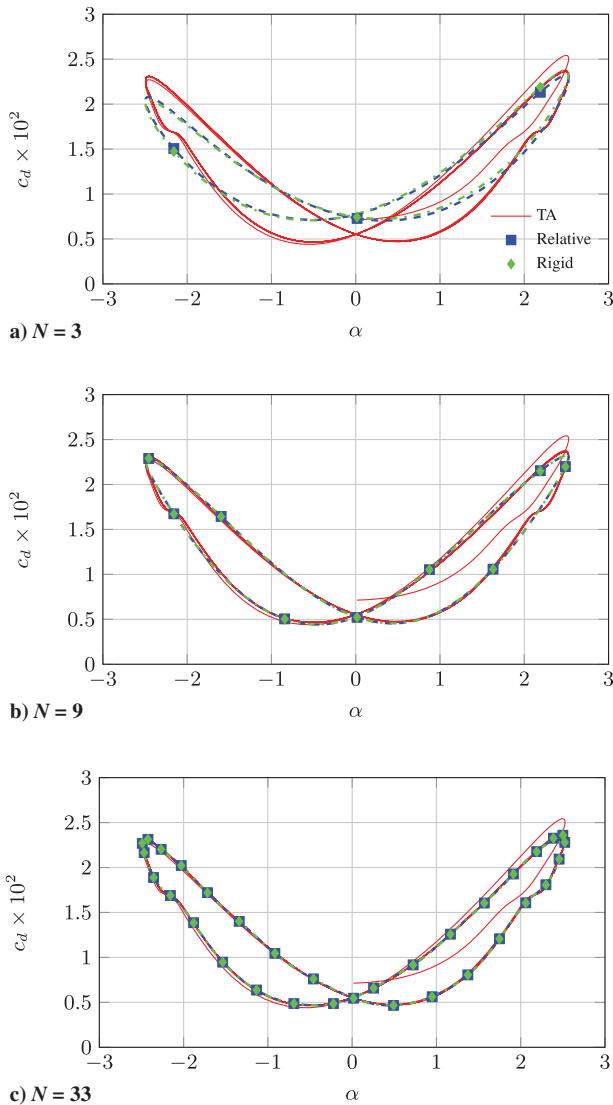


Fig. 15 Time-spectral vs time-accurate drag coefficients for $N \in \{3, 9, 33\}$ for rigid and relative motion. Corrected experimental drag data from the AGARD 702 report [46] are not available.

included in the experiment and previous computations, it is omitted in the current work.

The hover test case employs a uniform collective of 14 deg with a tip speed of $M_{\text{tip}} = 0.625$ and tip Reynolds number of $Re_{\text{tip}} = 2.1$ million, which is consistent with the primary TRAM test case in [50]. The laminar off-body procedure outlined by Potsdam and Pulliam [50] is employed for both hover and forward-flight cases. Qualitative results from both time-accurate and single-

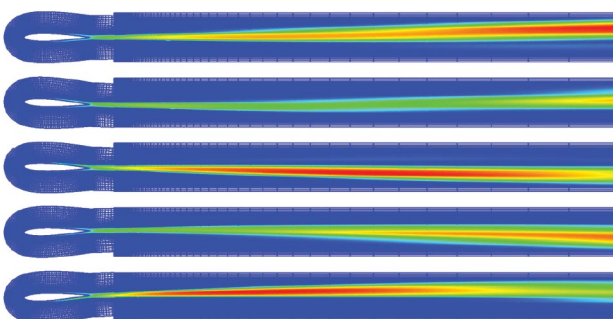


Fig. 16 Visualization of undamped turbulent eddy viscosity on the near-body grid and in the wake region at each time instance for a representative case of $N = 5$.

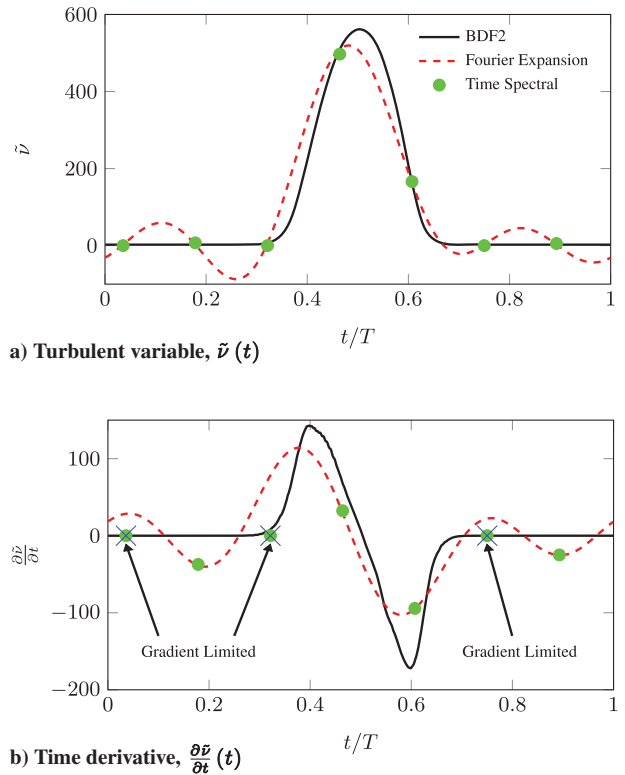


Fig. 17 Continuous and Fourier representation of a) the turbulent working variable \tilde{v} and b) its temporal derivative and locations where temporal gradient was limited.

harmonic ($N = 3$) time-spectral V-22 TRAM hover calculations are presented in Figs. 20 and 21. Figure 20 plots isocontours of vorticity magnitude, as well as a cutting plane of the same functional. Figure 21 plots the same isocontours of vorticity magnitude over a cutting plane of undamped eddy viscosity. The time-accurate and time-spectral calculations demonstrate strong qualitative agreement in both cases because the images are virtually indistinguishable.

Dozens of periods are required to achieve a fully periodic steady state and converge certain functionals of interest in a time-accurate hover calculation [53] because of the prolonged transients that persist due to a lack of a freestream flow. The time-spectral simulation is steady in nature and converges directly to the space-time solution. Furthermore, only a single mode must be resolved for hover (when all grids rotate with the blades), making the scheme particularly attractive for this flow configuration.

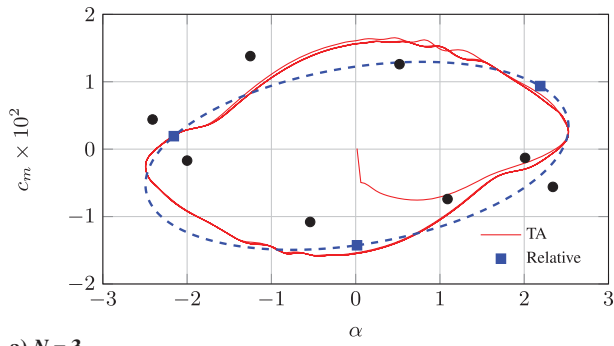
The figure of merit (FM) is an established scalar performance measure for rotorcraft in hover, gauging rotor efficiency as a ratio of the ideal power, derived from momentum theory, to the actual (computed) power:

$$\text{FM} = \frac{1}{\sqrt{2}} \frac{C_T^{3/2}}{C_Q} \quad (31)$$

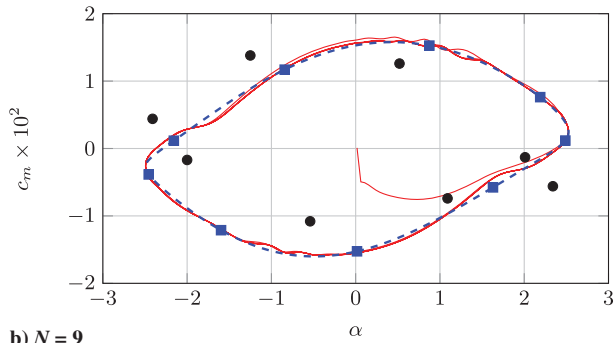
Table 1 provides the force and moment coefficients and the figure of merit for the time-accurate and single-harmonic time-spectral calculations; the FM values agree to within 5% of a percent. However, these FM values are substantially lower than those commonly reported [49–52]. This discrepancy is attributable to the use of only second-order central differencing of the convective terms, as opposed to higher-order schemes in the references cited.

2. Edgewise Flight

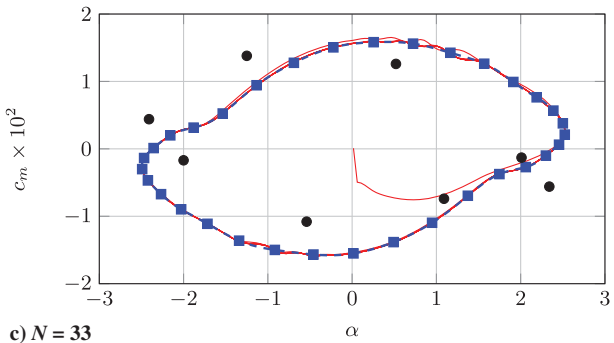
The hover case of the previous section prescribed the rigid motion of the isolated V-22 TRAM rotor with its off-body grid system, resulting in an absence of dynamically blanked nodes. Rotors in forward (edgewise) flight experience an imbalance of dynamic



a) $N = 3$



b) $N = 9$

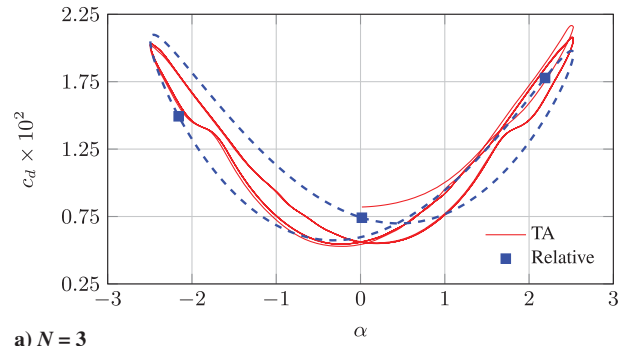


c) $N = 33$

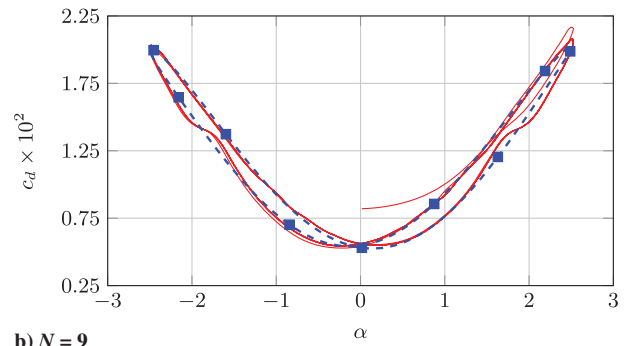
Fig. 18 Time-spectral vs time-accurate pitching-moment coefficients for $N \in \{3,9,33\}$ for relative motion. Experimental data from the AGARD 702 report [46] are plotted with black dots.

pressure on the advancing ($0 \leq \Psi \leq 180$) and retreating ($180 \leq \Psi \leq 360$) segments of the rotation. Left untreated, this leads to an undesired moment about the longitudinal axis of the vehicle. Cyclic pitch mitigates the force imbalance by dynamically varying the pitch amplitude of the blade. On the advancing side, where blades experience a higher dynamic pressure, pitch is decreased to reduce the resulting normal force. Conversely, blades pitch upward on the retreating side to increase the normal force in the presence of lower dynamic pressure. Although the Cartesian background grids are still prescribed to rotate with the rotor, the relative pitching motion between the blades and background grids introduces dynamically blanked nodes, thereby requiring the hybrid time-spectral scheme.

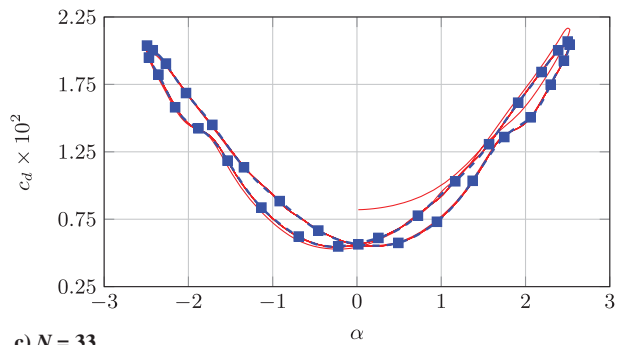
The V-22 tiltrotor is not typically operated in forward (edgewise) flight because its thrust is derived through a rotation of its rotors into propeller mode. However, the edgewise-flight case provides an opportunity to gauge the hybrid time-spectral method in three spatial dimensions. A reasonable selection of parameters has been chosen for the values of collective and cyclic pitch estimated from Young et al. [47] using a vertical shaft axis. Although the rotor is not trimmed with a comprehensive analysis tool, the prescription of cyclic pitch serves as a representative estimate of rotor trim and induces relative motion as desired.



a) $N = 3$



b) $N = 9$



c) $N = 33$

Fig. 19 Time-spectral vs time-accurate drag coefficients for $N \in \{3,9,33\}$ for relative motion. Corrected experimental drag data from the AGARD 702 report [46] are not available.

Time-accurate and time-spectral forward-flight V-22 TRAM calculations are presented for an advance ratio $\mu = 0.2$, where $M_\infty = \mu M_{tip}$, using the same tip Mach and Reynolds numbers as the hover case. The pitch amplitude $\theta(\Psi)$ is defined with a collective $\theta_0 = 10$ deg and longitudinal and lateral cyclic pitch amplitudes $\theta_{C1} = 3$ deg and $\theta_{S1} = -5$ deg, respectively:

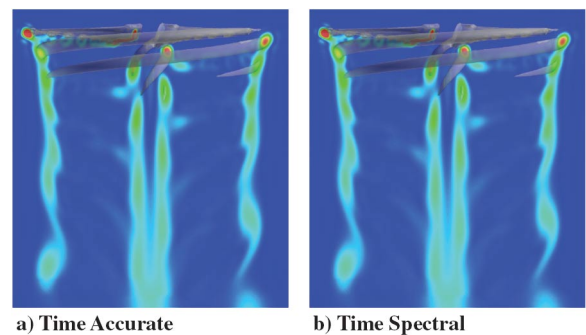


Fig. 20 Comparison of instantaneous isocontours of vorticity for time-accurate and time-spectral simulations. Contours of vorticity magnitude are plotted in a constant y plane.

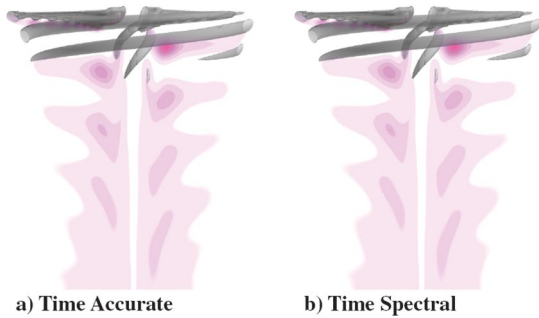


Fig. 21 Comparison of instantaneous isocontours of vorticity for time-accurate and time-spectral simulations. Contours of undamped turbulent eddy viscosity $\bar{\nu}$ are plotted in a constant y plane.

$$\theta(\Psi) = \theta_0 + \theta_{C1} \cos(\Psi) + \theta_{S1} \sin(\Psi) \quad (32)$$

The azimuthal angle Ψ is taken to be zero in the freestream direction. The off-body grid system is modified for the forward-flight case because vorticity shedding off of the rotor is convected downstream as opposed to straight down as in the case of hover. Thus, the Cartesian off-body grid system is compressed to provide a wider L1 grid near the rotor to capture vortical content as it convects downstream for a longer duration. The modified off-body grid system still contains a hierarchy of 46 isotropic Cartesian meshes with a total of 20.3 million grid points. Therefore, the entire grid system is composed of 26.1 million grid points, which is nearly equivalent to the amount used for hover. The L1 grid spans roughly $\pm 1.65R$ in both the x and y directions and $-0.9R$ and $+0.28R$ in the z direction, with the same spacing of $0.1c_{tip}$ as the hover case.

Qualitative comparisons between the time-accurate and time-spectral forward-flight results are evident in Figs. 22 and 23. Figure 22 plots isocontours of vorticity magnitude and a cutting plane of undamped eddy viscosity. The time-spectral solution using only 11 time samples shows some agreement with the time-accurate result but demonstrates marked disagreement in the turbulence variable. The time-spectral solution using 21 time samples offers significant improvement. Using 31 time samples resolves some of the finer features exhibited in the time-accurate result and provides improved agreement of the turbulent eddy viscosity field. Side views of the four cases, provided in Fig. 23, demonstrate similar trends. Unlike the case of hover, the flow is no longer steady in the rotating frame. The tip vortices being convected downstream pose a resolution problem for unsteady simulation as a point on the rotating background mesh moves quickly through the vortices. This is yet another example of a case where a relatively low-frequency disturbance in one frame is transformed to a much higher-frequency signal in another frame, which may explain the poor resolution of the tip vortices in the time-spectral calculations.

Finally, Fig. 24 demonstrates quantitative convergence of the time-spectral calculations to the time-accurate solution for the instantaneous thrust coefficient C_T versus azimuthal angle Ψ . Despite rather poor qualitative agreement, the time-spectral case using 11 time samples resolves the bulk C_T signal. Naturally, agreement improves with temporal refinement. The time-spectral result using 31 time samples matches the time-accurate signal over nearly the entire period.

In contrast to the case of hover, only a modest number of revolutions are required to achieve a periodic steady state using the time-accurate solver for the case of forward flight because of the addition of a nonzero freestream. This fact, coupled with the need to

Table 1 Force and moment coefficients and figure of merit for TA and single-harmonic TS calculations

	C_T	C_O	FM
TA	0.11383×10^{-1}	0.15320×10^{-2}	0.5605
TS	0.11379×10^{-1}	0.15320×10^{-2}	0.5602

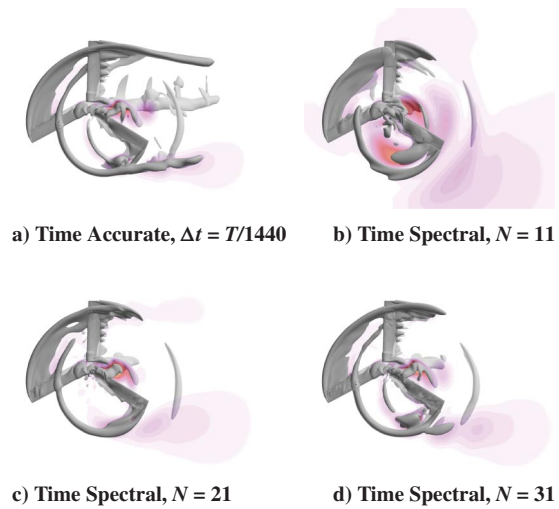


Fig. 22 Top view of instantaneous isocontours of vorticity for time-accurate and time-spectral calculations. Contours of undamped eddy viscosity are plotted in a constant z plane.

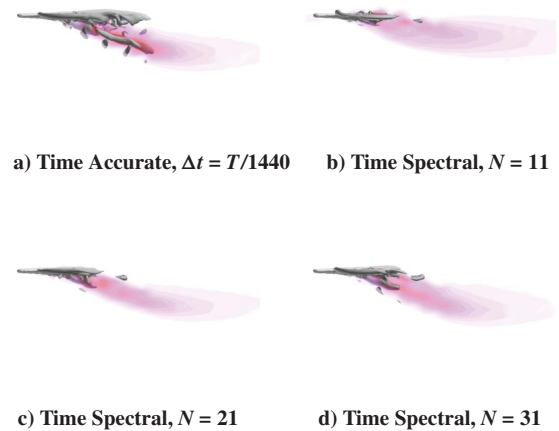


Fig. 23 Side view of instantaneous isocontours of vorticity for time-accurate and time-spectral calculations. Contours of undamped eddy viscosity are plotted in a constant y plane.

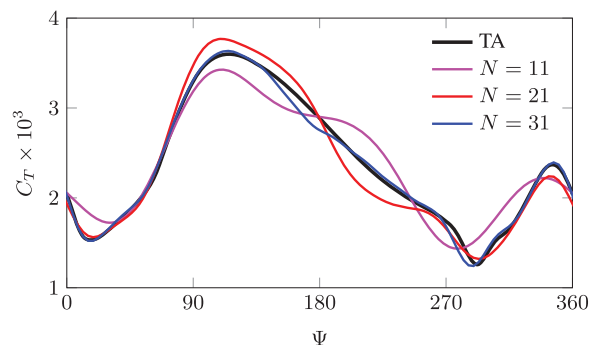


Fig. 24 Reconstruction of thrust coefficient C_T from time-spectral calculations with $N \in \{11,21,31\}$ vs the time-accurate solution using a quarter-degree time step $\Delta t = T/1440$.

resolve a significantly greater number of modes in the time-spectral calculation, suggests that the competitive advantage afforded by temporal pseudospectral methods is problem dependent and cannot universally reduce time-to-solution for periodic flows.

VI. Conclusions

A hybrid time-spectral method was developed to facilitate its use within an overset framework and its implementation within NASA's implicit OVERFLOW solver was outlined. The time-spectral augmented OVERFLOW solver was applied to high-amplitude inviscid and high-speed inviscid and turbulent oscillating airfoil cases. The high-amplitude plunging case validated the superior performance of the barycentric rational interpolant representation, in particular, to represent the aperiodic temporal variation on equispaced nodes for dynamically blanked nodes. It was also shown that the use of relative motion requires additional resolution in contrast to using rigid motion, as a consequence of the added frequency content induced by the motion. The proposed scheme was also capable of computing transonic, turbulent flow about an oscillating airfoil and three-dimensional flow about an isolated V-22 rotor in both hover and edgewise flight.

Acknowledgments

The authors would like to thank Roger Strawn and the U.S. Army Aviation Development Directorate for sponsoring this research and NASA Advanced Supercomputing Division for providing the computational resources.

References

- [1] Hall, K. C., Thomas, J. P., and Clark, W. S., "Computation of Unsteady Nonlinear Flows in Cascades Using a Harmonic Balance Technique," *Proceedings of the 9th International Symposium on Unsteady Aerodynamics, Aeroacoustics and Aeroelasticity of Turbomachines (ISUAAAT) and Legendre Lecture Series*, edited by P. Ferrand, and S. Aubert, Presses Universitaires de Grenoble, Lyon, France, Sept. 2000.
- [2] Hall, K. C., Thomas, J. P., and Clark, W., "Computation of Unsteady Nonlinear Flows in Cascades Using a Harmonic Balance Technique," *AIAA Journal*, Vol. 40, No. 5, May 2002, pp. 879–886. doi:10.2514/2.1754AIAJAH0001-1452
- [3] McMullen, M., and Jameson, A., "The Computational Efficiency of Non-Linear Frequency Domain Methods," *Journal of Computational Physics*, Vol. 212, No. 2, 2006, pp. 637–661. doi:10.1016/j.jcp.2005.07.021JCTPAH0021-9991
- [4] McMullen, M., Jameson, A., and Alonso, J., "Demonstration of Nonlinear Frequency Domain Methods," *AIAA Journal*, Vol. 44, No. 7, July 2006, pp. 1428–1435. doi:10.2514/1.15127AIAJAH0001-1452
- [5] Nadarajah, S. K., McMullen, M. S., and Jameson, A., "Optimum Shape Design for Unsteady Flows Using Time Accurate and Non-Linear Frequency Domain Methods," *AIAA Paper* 2003-3875, June 2003.
- [6] Murman, S. M., "Reduced-Frequency Approach for Calculating Dynamic Derivatives," *AIAA Journal*, Vol. 45, No. 6, June 2007, pp. 1161–1168. doi:10.2514/1.15758AIAJAH0001-1452
- [7] Van der Weide, E., Gopinath, A. K., and Jameson, A., "Turbomachinery Applications with the Time Spectral Method," *AIAA Paper* 2005-4905, June 2005.
- [8] Gopinath, A. K., and Jameson, A., "Time Spectral Method for Periodic Unsteady Computations over Two- and Three-Dimensional Bodies," *AIAA Paper* 2005-1220, Jan. 2005.
- [9] Gopinath, A. K., and Jameson, A., "Application of the Time Spectral Method to Periodic Unsteady Vortex Shedding," *AIAA Paper* 2006-0449, Jan. 2006.
- [10] Canuto, C., Hussaini, M., Quarteroni, A., and Zang, T., *Spectral Methods: Fundamentals in Single Domains*, Scientific Computation, Springer-Verlag, Berlin, 2006.
- [11] Thomas, J. P., Custer, C. H., Dowell, E. H., and Hall, K. C., "Unsteady Flow Computation Using a Harmonic Balance Approach Implemented About the OVERFLOW 2 Flow Solver," *AIAA Paper* 2009-4270, June 2009.
- [12] Thomas, J. P., Custer, C. H., Dowell, E. H., Hall, K. C., and Corre, C., "Compact Implementation Strategy for a Harmonic Balance Method Within Implicit Flow Solvers," *AIAA Journal*, Vol. 51, No. 6, June 2013, pp. 1374–1381. doi:10.2514/1.J051823AIAJAH0001-1452
- [13] Custer, C. H., "A Nonlinear Harmonic Balance Solver for an Implicit CFD Code: OVERFLOW 2," Ph.D. Thesis, Duke Univ., Durham, NC, 2009.
- [14] Blanc, F., Roux, F.-X., Jouhaud, J.-C., and Bousuge, J.-F., "Numerical Methods for Control Surfaces Aerodynamics with Flexibility Effects," *International Forum on Aeroelasticity and Structural Dynamics 2009*, Seattle, June 2009.
- [15] Soucy, O., and Nadarajah, S. K., "A NLFD Method for the Simulation of Periodic Unsteady Flows for Overset Meshes," *AIAA Paper* 2009-4271, June 2009.
- [16] Mavriplis, D. J., Yang, Z., and Mundis, N., "Extensions of Time Spectral Methods for Practical Rotorcraft Problems," *AIAA Paper* 2012-0423, Jan. 2012.
- [17] Choi, S., Potsdam, M., Lee, K., Iaccarino, G., and Alonso, J. J., "Helicopter Rotor Design Using a Time-Spectral and Adjoint-Based Method," *AIAA Paper* 2008-5810, Sept. 2008.
- [18] Mavriplis, D. J., and Yang, Z., "Time Spectral Method for Periodic and Quasi-Periodic Unsteady Computations on Unstructured Meshes," *AIAA Paper* 2010-5034, June 2010.
- [19] Peyret, R., *Spectral Methods for Incompressible Viscous Flow*, Applied Mathematical Sciences, Springer-Verlag, New York, 2002.
- [20] Hesthaven, J. S., Gottlieb, S., and Gottlieb, D., *Spectral Methods for Time-Dependent Problems*, Cambridge Monographs on Applied and Computational Mathematics, Cambridge Univ. Press, Cambridge, England, U.K., 2007.
- [21] Benek, J. A., Steger, J. L., and Dougherty, F. C., "A Flexible Grid Embedding Technique with Application to the Euler Equations," *AIAA Paper* 1983-1944-CP, 1983.
- [22] Leffell, J. I., Murman, S. M., and Pulliam, T. H., "An Extension of the Time-Spectral Method to Overset Solvers," *AIAA Paper* 2013-0637, Jan. 2013.
- [23] Maple, R. C., King, P. I., and Oxley, M. E., "Adaptive Harmonic Balance Solutions to Euler's Equation," *AIAA Journal*, Vol. 41, No. 9, Sept. 2003, pp. 1705–1714. doi:10.2514/2.7316AIAJAH0001-1452
- [24] Mosahebi, A., and Nadarajah, S., "An Adaptive Non-Linear Frequency Domain Method for Viscous Flows," *Computers & Fluids*, Vol. 75, April 2013, pp. 140–154. doi:10.1016/j.compfluid.2012.12.016
- [25] Strang, G., "The Optimal Coefficients in Daubechies Wavelets," *Physica D: Nonlinear Phenomena*, Vol. 60, Nos. 1–4, 1992, pp. 239–244. doi:10.1016/0167-2789(92)90240-NPDNPDT0167-2789
- [26] Romine, C. H., and Peyton, B. W., "Computing Connection Coefficients of Compactly Supported Wavelets on Bounded Intervals," *Mathematical Sciences Sec.*, Oak Ridge National Lab., ORNL/TM-13413, Oak Ridge, TN, April 1997.
- [27] Huybrechs, D., "On the Fourier Extension of Nonperiodic Functions," *SIAM Journal on Numerical Analysis*, Vol. 47, No. 6, 2010, pp. 4326–4355. doi:10.1137/090752456
- [28] Boyd, J. P., "A Comparison of Numerical Algorithms for Fourier Extension of the First, Second, and Third Kinds," *Journal of Computational Physics*, Vol. 178, No. 1, 2002, pp. 118–160. doi:10.1006/jcph.2002.7023JCTPAH0021-9991
- [29] Bruno, O. P., Han, Y., and Pohlman, M. M., "Accurate, High-Order Representation of Complex Three-Dimensional Surfaces via Fourier Continuation Analysis," *Journal of Computational Physics*, Vol. 227, No. 2, 2007, pp. 1094–1125. doi:10.1016/j.jcp.2007.08.029JCTPAH0021-9991
- [30] Candès, E. J., "Compressive Sampling," *Proceedings of the International Congress of Mathematicians*, Madrid, Spain, 2006.
- [31] Boyd, J. P., *Chebyshev and Fourier Spectral Methods*, 2nd ed., Dover, New York, 2001.
- [32] Platte, R. B., Trefethen, L. N., and Kuijlaars, A. B., "Impossibility of Fast Stable Approximation of Analytic Functions from Equispaced Samples," *SIAM Review*, Vol. 53, No. 2, 2011, pp. 308–318. doi:10.1137/090774707SIREAD0036-1445
- [33] Bos, L., De Marchi, S., Hormann, K., and Klein, G., "On the Lebesgue Constant of Barycentric Rational Interpolation at Equidistant Nodes," *Numerische Mathematik*, Vol. 121, No. 3, 2012, pp. 461–471. doi:10.1007/s00211-011-0442-8NUMMA70029-599X
- [34] Baltensperger, R., and Berrut, J.-P., "The Linear Rational Collocation Method," *Journal of Computational and Applied Mathematics*, Vol. 134, Nos. 1–2, 2001, pp. 243–258. doi:10.1016/S0377-0427(00)00552-5JCAMDIO377-0427
- [35] Berrut, J.-P., and Baltensperger, R., "The Linear Rational Pseudospectral Method for Boundary Value Problems," *BIT Numerical Mathematics*, Vol. 41, No. 5, 2001, pp. 868–879. doi:10.1023/A:1021916623407
- [36] Klein, G., "An Extension of the Floater-Hormann Family of Barycentric Rational Interpolants," *Mathematics of Computation*, Vol. 82, No. 284,

- Oct. 2013, pp. 2273–2292.
doi:10.1090/mcom/2013-82-284MCMPPAF0025-5718
- [37] Tee, T. W., and Trefethen, L. N., “A Rational Spectral Collocation Method with Adaptively Transformed Chebyshev Grid Points,” *SIAM Journal on Scientific Computing*, Vol. 28, No. 5, 2006, pp. 1798–1811.
doi:10.1137/050641296
- [38] Baltensperger, R., Berrut, J.-P., and Noël, B., “Exponential Convergence of a Linear Rational Interpolant Between Transformed Chebyshev Points,” *Mathematics of Computation*, Vol. 68, No. 227, Feb. 1999, pp. 1109–1121.
doi:10.1090/S0025-5718-99-01070-4MCMPPAF0025-5718
- [39] Floater, M. S., and Hormann, K., “Barycentric Rational Interpolation with No Poles and High Rates of Approximation,” *Numerische Mathematik*, Vol. 107, No. 2, Aug. 2007, pp. 315–331.
doi:10.1007/s00211-007-0093-yNUMMA70029-599X
- [40] Wang, Q., Moin, P., and Iaccarino, G., “A Rational Interpolation Scheme with Superpolynomial Rate of Convergence,” *SIAM Journal on Numerical Analysis*, Vol. 47, No. 6, 2010, pp. 4073–4097.
doi:10.1137/080741574
- [41] Leffell, J., “An Overset Time-Spectral Method for Relative Motion,” Ph.D. Thesis, Stanford Univ., Stanford, CA, June 2014.
- [42] Nichols, R., Tramel, R., and Buning, P., “Solver and Turbulence Model Upgrades to OVERFLOW 2 for Unsteady and High-Speed Applications,” AIAA Paper 2006-2824, June 2006.
- [43] Beam, R. M., and Warming, R., “An Implicit Finite-Difference Algorithm for Hyperbolic Systems in Conservation-Law Form,” *Journal of Computational Physics*, Vol. 22, No. 1, 1976, pp. 87–110.
doi:10.1016/0021-9991(76)90110-8JCTPAH0021-9991
- [44] Jameson, A., “Time Dependent Calculations Using Multigrid, with Applications to Unsteady Flows Past Airfoils and Wings,” AIAA Paper 1991-1596, June 1991.
- [45] McMullen, M. S., “The Application of Non-Linear Frequency Domain Methods to the Euler and Navier-Stokes Equations,” Ph.D. Thesis, Stanford Univ., Stanford, CA, March 2003.
- [46] Landon, R. H., “Compendium of Unsteady Aerodynamic Measurements,” AGARD Rept. 702, Aug. 1982.
- [47] Young, L. A., Booth, E. R., Jr., Yamauchi, G. K., Botha, G., and Dawson, S., “Overview of the Testing of a Small-Scale Proprotor,” *American Helicopter Society 55th Annual Forum*, Montreal, Canada, May 1999.
- [48] Swanson, S. M., McCluer, M. S., Yamauchi, G. K., and Swanson, A. A., “Airloads Measurements From a 1/4-Scale Tiltrotor Wind Tunnel Test,” *Proceedings of the 25th European Rotorcraft Forum*, Rome, Italy, Sept. 1999.
- [49] Potsdam, M. A., and Strawn, R. C., “CFD Simulations of Tiltrotor Configurations in Hover,” *Journal of the American Helicopter Society*, Vol. 50, No. 1, 2005, pp. 82–94; also *American Helicopter Society 58th Annual Forum*, Montreal, QC, June 2002.
doi:10.4050/1.3092845JHESAK0002-8711
- [50] Potsdam, M., and Pulliam, T., “Turbulence Modeling Treatment for Rotorcraft Wakes,” *AHS Specialist’s Conference on Aeromechanics*, Jan. 2008.
- [51] Chaderjian, N. M., and Buning, P. G., “High Resolution Navier–Stokes Simulations of Rotor Wakes,” *American Helicopter Society 67th Annual Forum*, Virginia Beach, VA, May 2011.
- [52] Chaderjian, N. M., “Advances in Rotor Performance and Turbulent Wake Simulation Using DES and Adaptive Mesh Refinement,” *Seventh International Conference of Computational Fluid Dynamics*, ICCFD7-3506, July 2012.
- [53] Yoon, S., Lee, H. C., and Pulliam, T. H., “Computational Analysis of Multi-Rotor Flows,” AIAA Paper 2016-0812, Jan. 2016.

M. R. Visbal
Associate Editor